Evaluation of CMIP6 DECK Experiments With CNRM-CM6-1

Aurore Voldoire, David Saint-Martin, Stéphane Sénési, B. Decharme, A. Alias, Matthieu Chevallier, Jeanne Colin, Jean-François Guérémy, M. Michou, Marie-Pierre Moine, et al.

▶ **To cite this version:**

Aurore Voldoire, David Saint-Martin, Stéphane Sénési, B. Decharme, A. Alias, et al.. Evaluation of CMIP6 DECK Experiments With CNRM-CM6-1. Journal of Advances in Modeling Earth Systems, 2019, 11 (7), pp.2177-2213. 10.1029/2019ms001683 . hal-02346111

HAL Id: hal-02346111
https://hal.science/hal-02346111v1

Submitted on 17 Sep 2020

HAL is a multi-disciplinary open access archive for the deposit and dissemination of scientific research documents, whether they are published or not. The documents may come from teaching and research institutions in France or abroad, or from public or private research centers.

L'archive ouverte pluridisciplinaire **HAL**, est destinée au dépôt et à la diffusion de documents scientifiques de niveau recherche, publiés ou non, émanant des établissements d'enseignement et de recherche français ou étrangers, des laboratoires publics ou privés.

JAMES | Journal of Advances in Modeling Earth Systems

RESEARCH ARTICLE
10.1029/2019MS001683

Special Section:
The CNRM Climate and Earth System Models for CMIP6

Evaluation of CMIP6 DECK Experiments With CNRM-CM6-1

A. Voldoire[1], D. Saint-Martin[1], S. Sénési[1], B. Decharme[1], A. Alias[1], M. Chevallier[1], J. Colin[1], J.-F. Guérémy[1], M. Michou[1], M.-P. Moine[2], P. Nabat[1], R. Roehrig[1], D. Salas y Mélia[1], R. Séférian[1], S. Valcke[2], I. Beau[1], S. Belamari[1], S. Berthet[1], C. Cassou[2], J. Cattiaux[1], J. Deshayes[3], H. Douville[1], C. Ethé[4], L. Franchistéguy[1], O. Geoffroy[1], C. Lévy[3], G. Madec[3,5], Y. Meurdesoif[6], R. Msadek[2], A. Ribes[1], E. Sanchez-Gomez[2], L. Terray[2], and R. Waldman[1]

[1]CNRM, Université de Toulouse, Météo-France, CNRS, Toulouse, France, [2]CECI, Université de Toulouse, CNRS, CERFACS, Toulouse, France, [3]LOCEAN-IPSL, Sorbonne Université-CNRS-IRD-MNHN, Paris, France, [4]Institut Pierre et Simon Laplace, Paris, France, [5]INRIA, Université Grenoble Alpes, CNRS, LJK, Grenoble, France, [6]IPSL/Laboratoire de Sciences du Climat et de l'Environnement, CEA-CNRS, Gif-sur-Yvette, France

Abstract This paper describes the main characteristics of CNRM-CM6-1, the fully coupled atmosphere-ocean general circulation model of sixth generation jointly developed by Centre National de Recherches Météorologiques (CNRM) and Cerfacs for the sixth phase of the Coupled Model Intercomparison Project 6 (CMIP6). The paper provides a description of each component of CNRM-CM6-1, including the coupling method and the new online output software. We emphasize where model's components have been updated with respect to the former model version, CNRM-CM5.1. In particular, we highlight major improvements in the representation of atmospheric and land processes. A particular attention has also been devoted to mass and energy conservation in the simulated climate system to limit long-term drifts. The climate simulated by CNRM-CM6-1 is then evaluated using CMIP6 historical and Diagnostic, Evaluation and Characterization of Klima (DECK) experiments in comparison with CMIP5 CNRM-CM5.1 equivalent experiments. Overall, the mean surface biases are of similar magnitude but with different spatial patterns. Deep ocean biases are generally reduced, whereas sea ice is too thin in the Arctic. Although the simulated climate variability remains roughly consistent with CNRM-CM5.1, its sensitivity to rising CO_2 has increased: the equilibrium climate sensitivity is 4.9 K, which is now close to the upper bound of the range estimated from CMIP5 models.

Key Points:
- Description of CNRM-CM6-1 model components, their coupling, and tuning procedures are described
- Historical simulations and DECK experiments are assessed
- Preindustrial simulation is stable and mean climate and variability in historical runs is realistic

Correspondence to:
A. Voldoire,
aurore.voldoire@meteo.fr

Citation:
Voldoire, A., Saint-Martin, D., Sénési, S., Decharme, B., Alias, A., Chevallier, M., et al. (2019). Evaluation of CMIP6 DECK experiments with CNRM-CM6-1. *Journal of Advances in Modeling Earth Systems*, *11*, 2177–2213. https://doi.org/10.1029/2019MS001683

Received 4 MAR 2019
Accepted 24 MAY 2019
Accepted article online 1 JUN 2019
Corrected 23 JUL 2019
Published online 11 JUL 2019

This article was corrected on 23 JUL 2019. See the end of the full text for details..

©2019. The Authors.
This is an open access article under the terms of the Creative Commons Attribution-NonCommercial-NoDerivs License, which permits use and distribution in any medium, provided the original work is properly cited, the use is non-commercial and no modifications or adaptations are made.

1. Introduction

CNRM and Cerfacs collaborate since the 1990s to develop state-of-the-art atmosphere-ocean coupled general circulation models for climate studies: the CNRM-CM suite. Since its origin, this model is based on the coupling via OASIS (Valcke et al., 2006) of ARPEGE-Climat (Déqué et al., 1994) atmospheric model, which included the ISBA scheme (Noilhan & Planton, 1989) for the land surface, with the OPA ocean model (Madec et al., 1998). This model was progressively enriched to include other climate components: the sea ice model GELATO (Salas Mélia, 2002), the externalized surface interface SURFEX (Masson et al., 2013), and the river routing scheme TRIP (Total Runoff Integrating Pathways, Oki & Sud, 1998). In preparation of the sixth phase of the Coupled Model Intercomparison Project (CMIP6, Eyring et al., 2016), the group has released an updated version, namely CNRM-CM6-1.

In comparison to its predecessor CNRM-CM5.1 (Voldoire et al., 2013), which was the basis for the CNRM-Cerfacs contribution to CMIP5, CNRM-CM6-1 (Figure 1) corresponds to a major update of its atmospheric and land surface components. It now embarks ARPEGE-Climat version 6.3 and SURFEX version 8.0, with fully revised physical parameterizations for the atmosphere (http://www.umr-cnrm.fr/cmip6/references) and the land surface (Decharme et al., 2019), respectively. All other model components were also updated to their newest respective version but with only limited changes in the choice of parameterizations involved. In CNRM-CM6-1, the ocean, sea ice, and river routing components are based respectively on NEMO version 3.6 (Madec et al., 2017), GELATO version 6, and a new TRIP version redeveloped at CNRM and called CTRIP (Decharme et al., 2019). The coupling software was also updated to OASIS3-MCT (Craig et al., 2017), which now allows for parallel exchanges of fields. A novelty of the

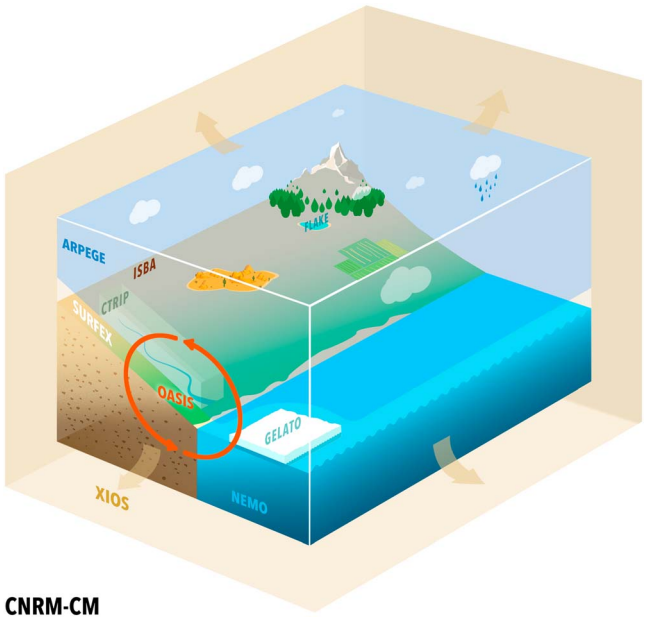

Figure 1. CNRM-CM6-1 components.

system is the inclusion of an output manager, the XIOS server (Meurdesoif, 2018), which allows efficient online output processing.

As a major update of CNRM-CM5.1, CNRM-CM6-1 is expected to better represent the climate system, both in terms of mean state and variability. It is intended that atmospheric processes are better represented by this drastic change in atmospheric parameterizations; however, this may not result in a general improvement of the model as experienced by other models, as shown, for example, by the version 5B of the IPSL-CM model (Hourdin et al., 2013). In this model, the change in atmospheric physics parameterizations led to an improvement of the tropical climate but a worsening of midlatitude and oceanic circulations (Dufresne et al., 2013). CNRM-CM5.1 takes benefit from a long history, which led to a fine tuning of the model, but also to several known or unknown compensations of errors. The main challenge in the course of CNRM-CM6-1 development was thus to achieve a satisfying model calibration in a rather short amount of time. This required work was, however, an opportunity to address this process in a more objective and comprehensive way, which will be detailed hereafter.

The purpose of this paper is to describe all components involved in CNRM-CM6-1 including the coupler setup and output server implementation (section 2). Section 3 details the calibration method followed, the forcing data set used to meet CMIP6 requirements, and the resulting drift obtained under constant preindustrial forcing. Section 4 assesses the mean state of the simulated climate, while section 5 addresses its variability. Finally, the model climate sensitivity is discussed in section 6. In sections 4 to 6, CNRM-CM6-1 is compared to CNRM-CM5.1 when applicable, to provide a comprehensive analysis of progresses made since the CMIP5 exercise. The last section summarizes the main skills and drawbacks of CNRM-CM6-1 and provides some perspectives. This paper aims to provide to the scientific community a general picture of CNRM-CM6-1, which is required to interpret results obtained within the multi-model framework encouraged by the CMIP panel. Additionally, CNRM-CM6-1 constitutes the core of the CNRM Earth System Model CNRM-ESM 2-1 designed to perform Earth system oriented Model Intercomparison Projects (MIPs) as part of CMIP6. It is also the base for a higher resolution version of CNRM-CM, namely, CNRM-CM6-1-HR.

2. Model Description

2.1. Atmospheric Component ARPEGE-Climat

The atmospheric component of CNRM-CM6-1 is based on the version 6.3 of the global atmospheric model ARPEGE-Climat. Its former version 5.2 has been described in Voldoire et al. (2013). A summary of the main characteristics of the new version is presented in the following with the emphasis on major updates. ARPEGE-Climat is a spectral model derived from the ARPEGE/IFS (Integrated Forecast System) numerical weather prediction model developed jointly by Météo-France and the European Center for Medium-range Weather Forecast. A linear triangular truncation Tl127 is adopted together with a corresponding reduced Gaussian grid (Hortal & Simmons, 1991). The model horizontal resolution is about 1.4° at the equator. The CNRM-CM6-1 atmospheric component has 91 vertical levels (31 for CNRM-CM5.1), following a progressive hybrid σ pressure discretization; the highest level is set at 0.01 hPa, while the boundary layer is described with about 15 levels below 1500 m.

The dynamical core is based on a two time level semi-Lagrangian numerical integration scheme tagged as cycle 37 of the ARPEGE/IFS system. A 15-min time step is used except for the radiative transfer module, which is called every hour. In addition to the six prognostic variables already considered in the previous version (vorticity, divergence, temperature, specific humidity, surface pressure, and ozone concentration), the model includes 10 new prognostic variables (cloud and precipitating solid and liquid water contents for both stratiform and convective parts, turbulent kinetic energy [TKE], and convective vertical velocity). As the semi-Lagrangian dynamical core is not fully conservative (Lucarini & Ragone, 2011), a global dry air mass and water conservation procedure are activated at each time step after application of a local correction to

the water condensates, following Bermejo and Conde (2002). Note that there is no correction applied on energy yet, such a development is planned for the next model version.

The same radiation parameterization as the one used in CNRM-CM5.1 is activated, that is, the Rapid Radiation Transfer Model (Mlawer et al., 1997) for the longwave part of the spectrum and a six-band shortwave scheme originally developed by Fouquart and Bonnel (1980). Some refinements were undertaken, including a new aerosol climatology (with revised optical properties and first indirect effect) based on an interactive aerosol simulation (paper in preparation). The cloud optical properties were also updated.

Compared to CNRM-CM5.1, the other atmospheric parameterizations correspond to a major update. The convection scheme follows the work of Piriou et al. (2007) and Guérémy (2011) and provides a continuous and prognostic treatment of dry, shallow, and deep convection. Convective microphysical processes are treated outside the convective scheme itself, in a consistent way with those occurring in the convection environment (see below). Entrainment and detrainment of energy, moisture, and microphysical species within the convective updraft depend on the prognostic updraft vertical velocity and follow a buoyancy sorting mechanism (Bretherton et al., 2004). The scheme closure is based on a dilute Convective Available Potential Energy (CAPE) relaxation. The stratiform microphysics scheme was designed following the work of Lopez (2002). It takes into account autoconversion, sedimentation, icing-melting, precipitation evaporation, and collection processes. Bouteloup et al. (2011) developed a probabilistic approach for the sedimentation, which allows longer time steps than those associated with the original lagrangian approach. The turbulence scheme follows the approach of Cuxart et al. (2000), which represents the turbulent kinetic energy with a 1.5-order scheme prognostic equation. The non-local mixing length is based on Bougeault and Lacarrère (1989). A specific treatment of the entrainment at the top of the boundary layer is taken into account based on Grenier and Bretherton (2001). The turbulence scheme also diagnoses the subgrid-scale variance of the saturation deficit, which depends on both the total water and liquid-water potential temperature turbulent fluctuations, and which is then used to compute the stratiform cloudiness and the cloud water content in a consistent way (Ricard & Royer, 1993; Sommeria & Deardorff, 1977). This diagnosed condensation rate serves as an input to the microphysics scheme. Finally, a non-orographic gravity wave drag parameterization was introduced in CNRM-CM6-1, following Lott et al. (2012), in addition to the orographic gravity wave drag counterpart which remains similar to that of CNRM-CM5.1 (Catry et al., 2008; Déqué et al., 1994).

2.2. Surface Component SURFEX

SURFEX is a numerical platform which simulates surface fluxes at the Earth's surface (Masson et al., 2013). It is coupled inline to ARPEGE-Climat and shares the same grid and time step. Three surface types are considered: land (including urban areas treated as rock surface), lakes, and ocean.

The land surface is represented using the new Interaction Soil-Biosphere-Atmosphere-CNRM TRIP (ISBA-CTRIP) coupled system (Decharme et al., 2019). ISBA calculates the time evolution of the energy and water budgets at the land surface, while CTRIP simulates river discharges up to the ocean from the total runoff computed by ISBA. CTRIP runs at a half degree resolution with a 30-min time step and is coupled to ISBA via the OASIS-MCT coupler (e.g., section 2.5). ISBA explicitly solves the one-dimensional Fourier and Darcy laws throughout the soil using 14 layers down to a 12-m depth and accounting for the hydraulic and thermal properties of soil organic carbon. The snow is represented by a 12 layer detailed internal process snow model including a simple ice sheet runoff to avoid unrealistic snow accumulation over continental glaciers. A two-way coupling between ISBA and CTRIP is set up to account for, first, a dynamic river flooding scheme in which floodplains interact with the soil and the atmosphere through free-water infiltration and evaporation and, second, a two-dimensional diffusive groundwater scheme to represent unconfined aquifers and upward capillarity fluxes into the superficial soil.

The land surface in one grid cell is tiled into 12 patches in order to account for the variety of soil and vegetation behaviors within a grid point. They aggregate the 500 land cover units at 1-km resolution present in the ECOCLIMAP-II database (Faroux et al., 2013). Mean seasonal cycles of both the snow-free albedo and the leaf area index are prescribed from Moderate Resolution Imaging Spectroradiometer products at 1-km spatial resolution. The soil textural properties (clay, sand, and soil organic carbon content) are given by the Harmonized World Soil Database (http://webarchive.iiasa.ac.at/Research/LUC/External-World-soil-

database/HTML/) at a 1-km resolution. Finally, the mean topography is derived from the 1-km Global Multi-resolution Terrain Elevation Data 2010 (https://topotools.cr.usgs.gov/gmted_viewer/). More details can be found in Decharme et al. (2019).

Lakes, including both the Caspian and the Aral seas, are represented using the bulk FLake model, which computes the temporal evolution of the vertical lake temperature profile from the surface mixing layer to the bottom. Modeled lakes can be covered with ice and snow. A skin temperature of a 1-mm thickness was introduced to simulate a surface temperature representative of the energy budget at the lake surface. The spatial distribution of lakes at the global scale is given by the ECOCLIMAP-II database, while the lake depth was specified from the 1-km Global Lake Depth database (Kourzeneva, 2010). More details can be found in Le Moigne et al. (2016). Note that FLake does not simulate the water mass evolution. The associated imbalance between precipitation, runoff, and evaporation over lake is thus artificially spread uniformly over the ocean.

Over the ocean, SURFEX resolves the exchange of momentum, energy, and water across the air-sea interface. The radiative properties of the seawater are handled by the ocean surface albedo scheme proposed by Séférian et al. (2018). The turbulent fluxes of momentum, heat, and water are computed using an improved version of the Exchange Coefficients from Unified Multi-campaigns Estimates (ECUME) scheme. It is a bulk iterative parameterization developed at CNRM from in situ measurements. This ECUME formulation is considered to better replicate the variability of the observed turbulent fluxes across a wide range of atmospheric and oceanic conditions.

2.3. Ocean Component NEMO

The ocean component of CNRM-CM6-1 is based on the version 3.6 of NEMO (Nucleus for European Models of the Ocean; Madec et al., 2017). It is based on the NOCS-ORCA1 configuration described in details in Danabasoglu et al. (2014). This configuration has been shared among climate modeling group through a dedicated NEMO project called “shaconemo” lead by Institut Pierre Simon Laplace (IPSL).

In CNRM-CM6-1, NEMO is run on eORCA1 horizontal grid, which is an extension of the ORCA1° tripolar grid already used in CNRM-CM5.1. The eORCA grids family differs from the ORCA grids family by the use of two quasi-isotropic bipolar grids south of 67°S instead of the former Mercator grid. The eORCA grids family allows for a more realistic representation of the contours of Antarctic ice shelves (Mathiot et al., 2017). In eORCA1, a nominal resolution of 1° is chosen with a latitudinal grid refinement of 1/3° in the tropics.

CNRM-CM6-1 resolves ocean dynamics on 75 vertical levels using a vertical z coordinate with partial step bathymetry formulation (Barnier et al., 2009). The model layer thickness increases from 1 m near the surface to 200 m at a depth of 6,000 m. The time step is 30 min. At the surface, the model uses the split-explicit nonlinear free surface formulation proposed by Shchepetkin and McWilliams (2005), with a variable volume. Seawater thermodynamics uses the Roquet et al. (2015) polynomial approximation of TEOS-10 (IOC et al., 2010). Therefore, Conservative Temperature and Absolute Salinity are the model prognostic variables.

Radiative transfer in the water column is resolved using a chlorophyll-dependent three-waveband scheme as described in Lengaigne et al. (2007) and Mignot et al. (2013), using a seasonal climatology of surface chlorophyll concentration derived from a former 60-year-long simulation run with NEMO-PISCES (e.g., Lee et al., 2016). A vertical profile of chlorophyll concentration is extrapolated from surface concentrations (Morel & Berthon, 1989).

As for the lateral physics, the isoneutral tracer diffusivity and the horizontal viscosity are parameterized as in NOCS-ORCA1 (Danabasoglu et al., 2014). Parameterization of vertical mixing is also similar, with the addition of the internal wave-induced mixing parameterization of de Lavergne et al. (2016) which uses the tidal dissipation climatology of de Lavergne et al. (2019). Finally, the eddy-induced circulation is parameterized with the Gent and Mcwilliams (1990) parameterization as in NOCS-ORCA1, and with the addition of the Fox-Kemper et al. (2011) submesoscale mixed layer eddy overturning scheme.

2.4. Sea Ice Component GELATO

Sea ice within CNRM-CM6-1 is represented by Gelato 6. Most upgrades from version 5 of the code (Chevallier et al., 2013; Voldoire et al., 2013) aimed at improving the overall consistency of the code (in

particular, salt, water, and energy conservation) and increasing its computational efficiency. In contrast with Gelato 5, Gelato 6 is a fully parallel code. It is embedded within NEMO, has the same horizontal grid, and inherits the global domain decomposition of the ocean code.

Within the standard configuration of CNRM-CM6-1, Gelato has a time step of 3,600 s. It is used with five ice thickness categories, based on the World Meteorological Organization classification (less than 0.30, 0.3–0.7, 0.7–1.2, 1.2–2, and over 2-m thick). In each ice category, the snow is treated with a single layer, while ice is simulated with a nine-layer vertical discretization. The sea ice enthalpy formulation is based on Notz (2005). As in Hunke and Lipscomb (2010), an iterative method is used to solve the vertical heat diffusion equation in sea ice. The solar radiative transfert scheme through the snow pack covering sea ice was upgraded following Grenfell and Maykut (1977). Albedo of dry snow, melting snow, and melting ice are model parameters, set to 0.88, 0.77, and 0.58 in CNRM-CM6-1, respectively.

The elastic-viscous-plastic sea ice rheology implemented by Bouillon et al. (2009) on an Arakawa C-grid is used, consistently with the formulation of NEMO finite difference scheme, whereas it was solved on an Arakawa B-grid in Gelato 5. The sea ice transport follows an incremental remapping scheme based on an Arakawa-B formulation by Hunke et al. (1997). It was adapted to an Arakawa C-grid according to previous work from M. Bentsen to ensure a better consistency between the dynamics and transport, which is crucial to represent sea ice transport through one-grid-cell-wide straits. The transported variables are snow density, volume and enthalpy, and ice surface, volume, enthalpy, salinity, and age. Depending on sea ice thickness, rafting, and ridging may take place in case of sea ice convergence, as described in Salas Mélia (2002).

Some aspects of the ice-ocean interface were revised. In the quadratic bulk formula used to calculate the ice-ocean stress for ice-ocean momentum exchanges, the drag coefficient is set to 0.001. This value is higher to that used in CNRM-CM5.1 and other models (e.g., Vancoppenolle et al., 2009), in order to take into account that the top ocean level now resides within the relatively thin surface layer (~1- to 3-m thick), following Roy et al. (2015). The chosen value is a compromise between this rationale and stability constraints. The oceanic heat flux at ice bottom derives from McPhee (1992).

2.5. Coupling With OASIS

The model components are coupled using the OASIS3-MCT software (Craig et al., 2017), which implements exchanges between multiple executables running concurrently using Message Passing Interface (MPI) communication. The OASIS3-MCT approach has the advantage of requiring a minimal amount of modifications in existing component codes. In CNRM-CM6-1, OASIS3-MCT transfers and interpolates coupling fields between SURFEX, CTRIP, and NEMO at a coupling frequency of 1 hr. In contrast ARPEGE-Climat and SURFEX models are coupled inline, that is, SURFEX is called as a subroutine of ARPEGE-Climat at each atmospheric time step, and are thus considered as one executable by OASIS3-MCT. Similarly, NEMO and GELATO are also coupled inline at a 1-hr frequency.

NEMO sends the ocean and sea ice surface properties (sea surface temperature and currents, sea ice fraction and sea ice albedo) that are used in SURFEX to calculate surface turbulent and radiative fluxes, which are then sent back to NEMO. The same is done for the water cycle; SURFEX sends all runoffs and all floodwater relative fluxes to CTRIP. In turn, CTRIP returns back to SURFEX the groundwater table depth and its grid cell coverage and routes continental water runoff to the ocean. When entering NEMO, river discharges are spread vertically depending on the flow intensity to a maximum depth of 10 m. Additionally, SURFEX provides a net water budget over continental ice sheets and lakes to NEMO to close the water budget. This water from the Greenland ice sheet and lakes is incorporated at the ocean surface globally, whereas the Antarctic ice sheet water excess is only spread south of 60S.

The energy associated to water fluxes is taken into account in NEMO/GELATO. Liquid precipitation, evaporation, and river discharges enthalpy is calculated considering that they are given at sea surface temperature. Similarly, ice sheets water flux and snow falls are considered to be solid, with a 0 °C temperature; thus, the enthalpy flux corresponding to the melting of ice/snow is considered.

As the SURFEX tiling approach considers land, ocean, and lake surfaces to calculate fluxes, NEMO only receives the flux component computed over the ocean fraction of the grid cell. Due to ocean coastline mismatch between NEMO and SURFEX, a global conservation procedure is applied at each coupling time step to ensure energy and water conservation in the coupled system.

More details about the OASIS3-MCT implementation in SURFEX can be found in Voldoire et al. (2017).

2.6. Output Server XIOS

CNRM-CM6-1 is used in a large number of MIPs, which request numerous diagnostics to be output following specific format norms. In order to ease their production, the model was interfaced with XIOS (Meurdesoif, 2018), an input/output parallel server software allowing for a declarative description of output files content and for the realization of online operations on fields, thereby almost fully removing the need for postprocessing.

Once the distribution of the full model grid among processes is described, the XIOS library has a main interface routine (send_field), which allows each model MPI process to deliver easily its part of the full grid for any field. The routine send_field can be called from any model routine.

XIOS postprocessing operations include time sampling and averaging, spatial remapping and reduction, vertical interpolation, and simple arithmetics. They are configured at run time using a XML syntax. The processing is actually shared between the model MPI tasks and a number of XIOS additional MPI tasks, called servers. Two levels of servers are used to aggregate and redistribute the parallel output fields so that any given field is gathered into one file written to disk by one single MPI task (thus avoiding parallel writing). Special care was taken in XIOS to overlap model computation and input/output operations using communication buffers and thus to allow for scaling at high number of cores.

This approach is highly efficient compared to the classical offline post-processing approach, especially in the case of CMIP6 Data Request (DR), which combines 248 experiments. The DR involves 1,274 geophysical variables, which can be invoked in 44 so-called MIP tables, thus leading to 2027 "CMOR variables" covering a variety of spatial shapes and frequencies. An additional tool, called dr2xml (https://github.com/senesis/dr2pub), translates the CMIP6 DR for each year of each experiment in a set of XIOS conformant XML definitions. These definitions are then used to activate the outputs in CNRM-CM6-1 components, which are all XIOS-enabled thanks to an alias table mapping model variable names and CMIP6 DR variable names. At run time, CNRM-CM6-1 then creates NetCDF output files, which are directly conformant with CMIP6 requirements and ready to publish on the Earth System Federated Grid (ESGF), except for some climatologies. This approach is applicable to any other model as long as it uses XIOS to produce its outputs. It is currently used in the IPSL climate model for its CMIP6 production.

3. Model Setup for the DECK Experiments

3.1. Tuning Strategy

The calibration strategy applied for CNRM-CM6-1 followed the three main steps defined by Hourdin et al. (2017). The first step consists in choosing the model formulation for each of its components, mainly their targeted horizontal and vertical resolutions and set of parameterizations. In the case of the new parameterizations introduced in each component, component working groups (ocean, atmosphere, and land surface) performed calibration using idealized or in situ 1-D cases (see corresponding papers).

The second phase of tuning was based on stand-alone simulations of each component, to address the interactions between parameterizations and between parameterizations and the other component elements (e.g., dynamics).

For the oceanic component, OMIP simulations were performed and the calibration was carried out in strong collaboration with the shaconemo group. For CNRM-CM6-1, a specific aspect is the use of the GELATO sea ice model; additional tuning was thus made on sea ice melting albedo and drag under sea ice.

For the land/atmosphere component, simulations using the Atmospheric Model Intercomparison Project (AMIP) protocol were performed with interactive land surface and prescribed observed sea surface temperatures and sea ice cover; the present-day period, corresponding to years 1979–2014, was used. The zero-order metrics for these atmosphere-only simulations were the globally averaged top-of-the-atmosphere and surface energy balances. A second class of targets addressed the mean climate and covered climatological spatial maps of the main climate state variables (e.g., temperature, precipitation, surface pressure, and cloud radiative effects). A focus was also put on the precipitation daily distribution. An empirical iterative method was

used to tune the parameters relative to cloud and radiative processes (convective entrainment, autoconversion, and inhomogeneity scaling factor for SW and LW cloud optical thickness).

In the third and last step, coupled ocean-atmosphere simulations under fixed forcings and starting from observed oceanic conditions were carried out. The final objective was to prevent global-mean sea surface temperature (SST) of the coupled system from drifting by targeting a net surface energy balance on the ocean surface close to 0 W/m^2 after a spin-up phase. AMIP-type simulations were used to reach this zero imbalance at a reduced computational cost. The net energy flux entering the ocean corresponds to the sum of surface turbulent, radiative and enthalpy fluxes associated with water mass exchanges (mainly from runoff). These enthalpy fluxes are not diagnosed in AMIP type simulations. They were estimated from coupled simulations to 0.8 W/m^2. By accounting for these additional fluxes, the target surface energy balance in a fixed SST experiment must be roughly -0.8 W/m^2 for the Earth to be considered in radiative equilibrium. We focus here on the net surface energy balance rather than the top-of-the-atmosphere energy budget knowing that the atmospheric model is not fully conservative and considering the numerical energy sink of the atmosphere. Furthermore, the Earth is not presently in radiative equilibrium with a global mean imbalance of the order of 0.5 W/m^2 (as estimated by Hansen et al., 2011, for the recent 2000–2004 period). Therefore, the final AMIP target was fixed to about -0.3 W/m^2. To perform this final tuning of the radiative imbalance in AMIP and then coupled configurations, only one parameter (shortwave inhomogeneity scaling factor) was modified, in order to prevent overtuning (Dommenget & Rezny, 2018). This parameter mainly modifies the SW term and allows to reach global energy balance without modifying much the main properties obtained in the previous steps.

3.2. Forcings

In its CMIP6 modeling setup, CNRM-CM6-1 uses, unless otherwise detailed below, the suite of external forcing and boundary conditions recommended by Eyring et al. (2016), that is, the version 6.2 data collection release.

Greenhouse gases (GHG) concentrations are the yearly global averages of Meinshausen et al. (2017) for CO_2, N_2O, CH_4, CFC12 and a CFC11eq species that includes the effect of all the other GHG of the original data set (39 species); this grouping corresponds to option 2 of Meinshausen et al. (2017). Yearly global averages of the total solar irradiance forcing were similarly used (Matthes et al., 2017), as for CNRM-CM5.1. Additionally, a geothermal heating flux is applied at the ocean floor (Emile-Geay & Madec, 2009): it varies spatially, is constant in time, and has a global mean value of 86.4 mW/m^2.

As in CNRM-CM5.1, CNRM-CM6-1 uses monthly averages of aerosol optical depth (AOD) for five tropospheric aerosol categories (sulfate, black carbon, organic matter, sea salt, and dust) and one stratospheric aerosol category to represent their interactions with radiation and clouds. These AODs are vertically distributed using a fixed profile for each category. AODs of tropospheric aerosols were precomputed based on an AMIP-type simulation in which the Tropospheric Aerosols for ClimaTe In CNRM-CM (TACTIC) interactive aerosol scheme (as detailed in Michou et al., 2015) is activated. This simulation is driven by the CMIP6 surface emissions of anthropogenic and biomass burning emissions of short-lived climate forcers and CMIP6 AMIP SSTs and sea ice cover and covers the period from 1850 to 2014. To remove the effect of model internal variability, simulated monthly AODs of the five aerosol tropospheric species were low-pass filtered by applying a 11-year moving average. In CNRM-CM5.1, the Szopa et al. (2013) aerosol AODs were used. For CNRM-CM6-1, the method employed ensures more consistency first between the aerosol forcing and the atmospheric model climate and second between CNRM-CM6-1 and its Earth System Model (ESM) counterpart (Watson et al., 2018).

For the stratospheric aerosols, mainly emitted by volcanic eruptions, CNRM-CM6-1 uses the official CMIP6 data set adapted for the 550-nm wavelength (Thomason et al., 2018). The main differences with the Ammann et al. (2007) data set used in CNRM-CM5.1 occur during the 19th century, where volcanic eruption peaks are different. During the twentieth century, the main eruptions are quite similar in both data sets, even if the intensity and the length of the eruptions may change. The CMIP6 data set also includes a significant stratospheric aerosol concentration background that was not present in Ammann et al. (2007).

As presented in Figure 2 (bottom), the preindustrial tropospheric AOD in CNRM-CM6-1 is close to the one in CNRM-CM5.1, but the increase during the historical period is weaker, albeit in the range of the CMIP5

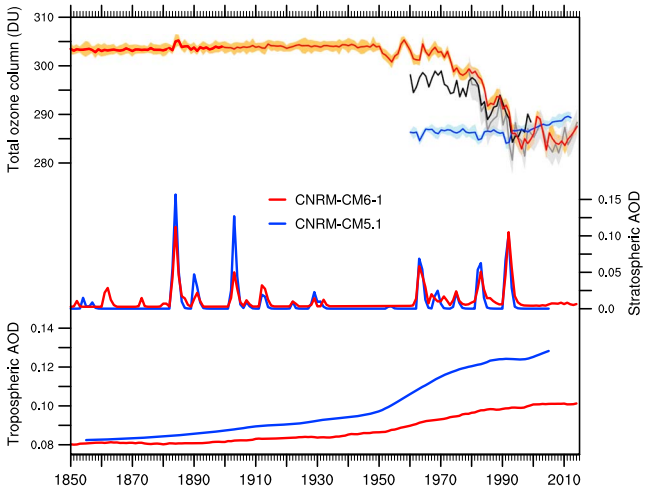

Figure 2. Area-weighted annual global means of total ozone column (DU, top), stratospheric (middle) and tropospheric (bottom) aerosol optical depth (AOD) at 550 nm used in the historical simulations of CNRM-CM5.1 (blue) and CNRM-CM6-1 (red). For the total ozone column, the NIWA3.3 data set (1980–2010, update of Bodeker et al., 2005) is in gray line, the CMIP6 ozone data set in black line, and the 90% confidence level has been added in colors based on the spread coming from the ensemble of 10 historical members in CNRM-CM5.1 and CNRM-CM6-1.

ensemble AOD (see Figure 9.29 in Flato et al., 2013). This is explained by two factors. First, the contribution of natural aerosols, especially sea salt particles, is stronger in CNRM-CM6-1 than in CNRM-CM5.1, while it is the opposite for sulfate aerosols. Second, over the twentieth century, the sulfate AOD increase is weaker in CNRM-CM6-1. Note that observations cannot constrain it yet over the whole historical period (Carslaw et al., 2017).

The ozone treatment has been marginally updated since CNRM-CM5.1 where the evolution of the ozone mixing ratio is computed following the Cariolle and Teyssèdre (2007) linear ozone parameterization. In CNRM-CM6-1, the parameterization remains linear, but recommendations of Monge-Sanz et al. (2011) have been followed so as to include implicitly heterogeneous chemistry in the scheme coefficients. As for AODs, monthly mean coefficients of the linear ozone parameterization have been computed from preliminary AMIP-type runs of ARPEGE-Climat 6.3 in which the interactive chemistry scheme REPROBUS (see Morgenstern et al., 2017, for details) is activated from 1950 to 2014 (a three-member ensemble has been considered). In CNRM-CM6-1, coefficients before 1950 are those of 1950. This approach also ensures a high consistency in the ozone representation between CNRM-CM6-1 and its ESM version.

CNRM-CM6.1 total ozone column (TOC, Dobson unit, DU) now agrees well with the two reference data sets over the 1980–2000 period, in terms of both absolute values and trend (Figure 2, top). This was a clear deficiency of CNRM-CM5.1, as reported in Eyring et al. (2013). Before 1960, the CNRM-CM6-1 TOC is overestimated by about 5 DU compared to the CMIP6 reference (https://esgf-node.llnl.gov/search/input4mips/). This bias is mainly driven by tropical regions. It is of opposite sign in the northern latitudes (a too weak Brewer-Dobson circulation could then compensate the positive bias of the tropics).

CNRM-CM6-1 uses a time-invariant distribution of land-cover, which is based on ECOCLIMAP-II (Faroux et al., 2013), and thus does not follow the recommendation of Eyring et al. (2016) to account for land use and land cover change forcings. In absence of a fully resolved carbon cycle, the relevance of land cover change can be questioned. Besides, the impact of land cover changes on surface radiative balance remains small with respect to the other forcings (Myhre et al., 2013, IPCC AR5).

In the following, the preindustrial simulation (known as piControl) of CNRM-CM6-1 uses time-invariant 1850 forcings for GHG, AOD, and ozone coefficients, whereas a present-day land cover state (taken as an average around the 2000s) is imposed. The simulation of the industrial era climate (as known as historical) uses the observed evolution of these forcings from 1850 to 2014 except for the land cover which is fixed to its present-day distribution.

3.3. Spin-up Initialization and Equilibrium State

In the development of CNRM-CM5.1, water conservation was an important focus, which resulted in a weak drift of the model ocean water mass (Table 1). However, salt conservation remained an issue, with a relatively high salinity drift of −0.01 psu/century in the ocean (Table 1; Gupta et al., 2013). In CNRM-CM6-1,

Table 1
Global Mean Tendencies Estimated by a Linear Regression Over 1,000 Years of piControl in CNRM-CM6-1 and 850 Years in CNRM-CM5.1; All Trends Are Statistically Significant

Trends	Near surface atmospheric temperature (K/century)	Sea water potential temperature (3-D; K/century)	Sea water salinity (3-D; psu/century)	Sea water mass (m/century)
CNRM-CM5.1	0.009	0.04	−0.01	−0.26
CNRM-CM6-1	0.02	0.03	-5.10^{-5}	0.009

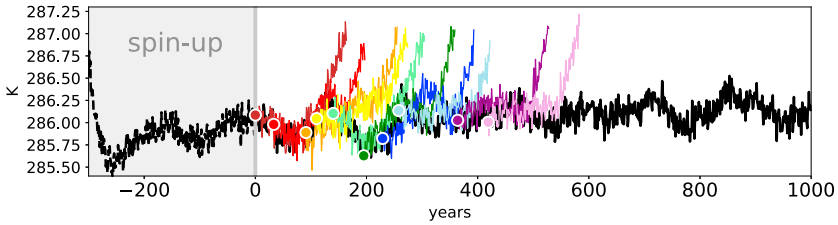

Figure 3. Global annual mean surface air temperature (K) evolution for the CNRM-CM6-1 piControl experiment over 1,000 years in black and for the 10 members historical experiments in colors; dots indicate the first-year annual mean for each historical simulations, respectively.

a specific effort has been made to ensure the conservation of water and salt in each component and in the coupling procedure. Concerning energy, all components with the noticeable exception of the atmosphere are conservative. In the atmospheric model ARPEGE-Climat, the effects of physical parameterizations are expressed in a flux-conservative formalism and therefore the physics is intrinsically conservative for mass and energy. But, as mentioned earlier, the semi-Lagrangian dynamical core does not ensure energy conservation and no "energy fixer" has been implemented yet in ARPEGE-Climat. However, under fixed conditions, the model should reach an equilibrium state after a spin-up phase.

Tuning is aimed at limiting the spin-up drift before reaching equilibrium, so that the final state remains close to the observed one. The model spin-up has been run under fixed preindustrial conditions corresponding to piControl CMIP6 forcings. The ocean component starts from the World Ocean Atlas 2013 (WOA, Locarnini et al., 2013). The initial sea ice concentration is set to 100% and its surface temperature at −10 °C where sea surface temperature is at freezing point. The sea ice thickness is initialized to 2 m in the Arctic and 1 m in the Antarctic. The initial thickness of the snow layer upon sea ice is set to zero. The land surface reservoirs are initialized from an equilibrium state obtained by running SURFEX in offline mode forced by atmospheric fields taken from a preindustrial AMIP simulation with ARPEGE-Climat.

Figure 3 illustrates the two-step behavior of the CNRM-CM6-1 spin-up: it is particularly strong and rapid during the first 100 years, which are then followed by a weak warming trend in global surface air temperature (GSAT). The warming trend is still present in the piControl experiment but limited to 0.02 K/century. The most noticeable feature is a large multidecadal variability superimposed on this trend. This feature will be discussed further in section 5, dedicated to variability. Averaged over the 1,000 years of the piControl simulation, the net heat flux over the ocean is 0.15 W/m^2; thus, CNRM-CM6-1 has not reached equilibrium. This imbalance is consistent with a global sea water potential temperature trend of 0.03 K/century. Compared to CNRM-CM5.1, the trend in the global mean sea water salinity is significantly reduced. Similarly, the top of the atmosphere imbalance is reduced from 3.6 W/m^2 in CNRM-CM5.1 to 1.5 W/m^2 in CNRM-CM6-1. This confirms that CNRM-CM6-1 better conserves energy and mass than its former version.

4. Modern Mean Climate Evaluation

In this section, we assess the performance of CNRM-CM6-1 to replicate modern observations and compare its skill to that of CNRM-CM5.1. The four major components of the climate system are assessed: atmosphere, land, ocean, and sea ice. In the following analysis, unless otherwise stated, we have used the 10-member ensemble historical simulations available for both model versions and focused on the 30 years period 1981–2010 to compare with observational or reanalysis data over the same period. In some cases, the period has been restricted to match with the period of availability of reference data sets. Details on the observationally derived data sets have been grouped in Appendix A.

4.1. Atmosphere

As the atmosphere component parameterizations have been fully revised in CNRM-CM6-1, a thorough evaluation of the atmospheric representation will be done in a forthcoming paper based on the analysis of the AMIP DECK experiment (http://www.umr-cnrm.fr/cmip6/references). Here, we summarize mainly the mean surface biases that could be affected by the coupling with the other components.

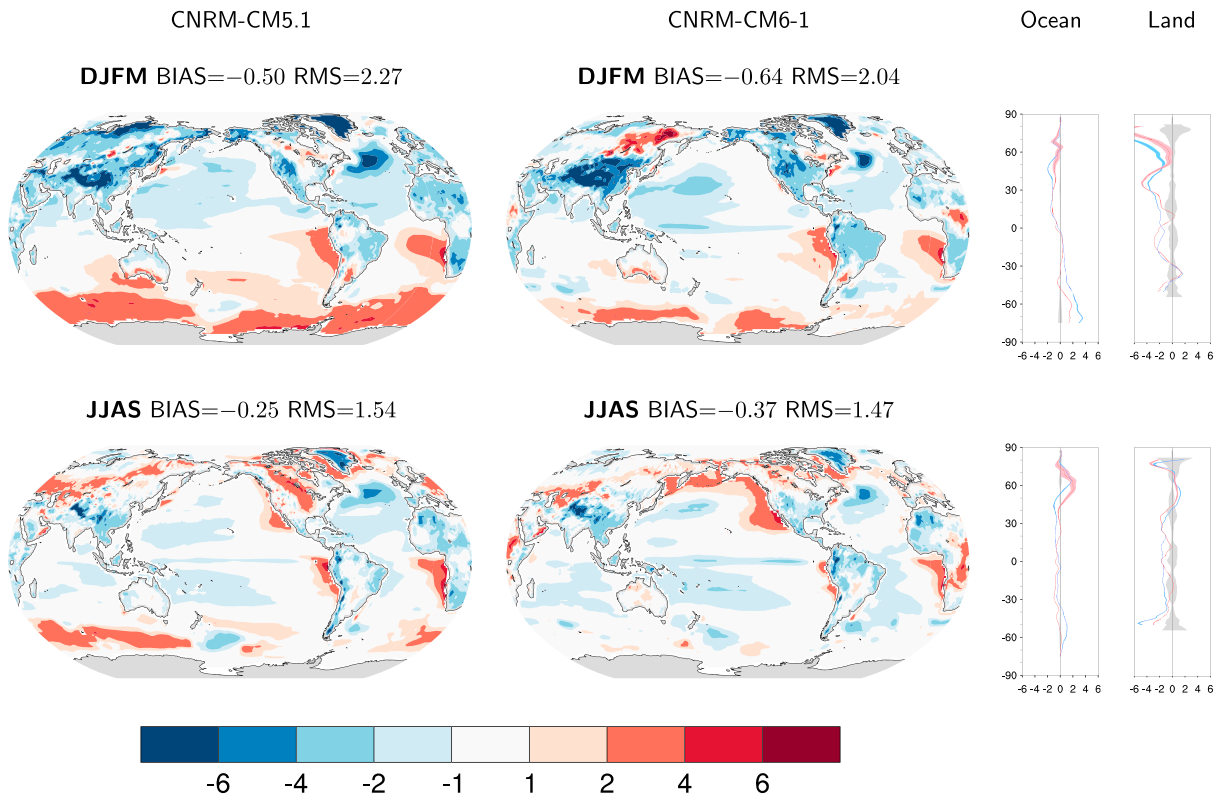

Figure 4. Biases (K) in surface air temperature over land and of sea surface temperature over oceans for CNRM-CM5.1 (first column) and CNRM-CM6-1 (second column) in December–March (DJFM; top row) and June–September (JJAS; bottom row). Biases are estimated as the difference between ensemble means of model historical simulations averaged over 1981–2010 and the average of several data sets over the same period. Details on observation products used can be found in Appendix A. Zonal mean errors over ocean (third column) and land (last column) show the inter-member range (±1,64 times the inter-member variance) for simulations in red (resp. blue) color shading for CNRM-CM6-1 (resp. CNRM-CM5.1) and the range of data for observational estimates in gray shading.

Overall, the surface temperature — air temperature (TAS) over land and SST over the ocean — exhibits rather similar patterns of biases in CNRM-CM5.1 and CNRM-CM6-1 (Figure 4).

Over the ocean, the most striking change between the two models occurs in the Southern Ocean where the warm bias of CNRM-CM5.1 has been significantly reduced in CNRM-CM6-1 in both seasons. This improvement is probably due to the increase in the shortwave cloud radiative effect over this region (Figure 6). This warm bias is relatively common in CMIP models (Wang et al., 2014) and has been shown to have an impact on tropical mean climate (Cabré et al., 2017; Mechoso et al., 2016); we may thus expect that this regional improvement may provide benefits on other regions in the model.

The warm biases in the eastern tropical ocean basins associated with a deficit in stratiform low clouds is weakly reduced except over the tropical north Pacific during boreal summer. Note that the bias in this region significantly varies among the 10-member ensemble, which possibly indicates a role of the ocean circulation. This type of SST warm bias is systematic to many climate models (Hourdin et al., 2015; Richter, 2015) and several origins have been pointed out in the literature (Zuidema et al., 2016, and references herein). The lack of stratiform low clouds over these regions is probably instrumental in CNRM-CM6-1(Brient et al., 2019). Compared to CNRM-CM5.1, the CNRM-CM6-1 low-cloud cover is improved (Figure 6) but the associated radiative effect has been tuned down to limit the so-called “too few-too bright” compensation error (Nam et al., 2012). Besides, Brient et al. (2019) show that the low-cloud cover still remains underestimated, due to deficiencies in the cloud parameterization itself and to slower feedbacks involving the large-scale circulation.

Over continents, CNRM-CM5.1 and CNRM-CM6-1 mostly show cold biases during the boreal winter (December–March). These biases are stronger in CNRM-CM6-1 over the Himalayas, with a wider pattern of cold bias. Over Greenland, the cold bias is slightly reduced in CNRM-CM6-1 (note that the values

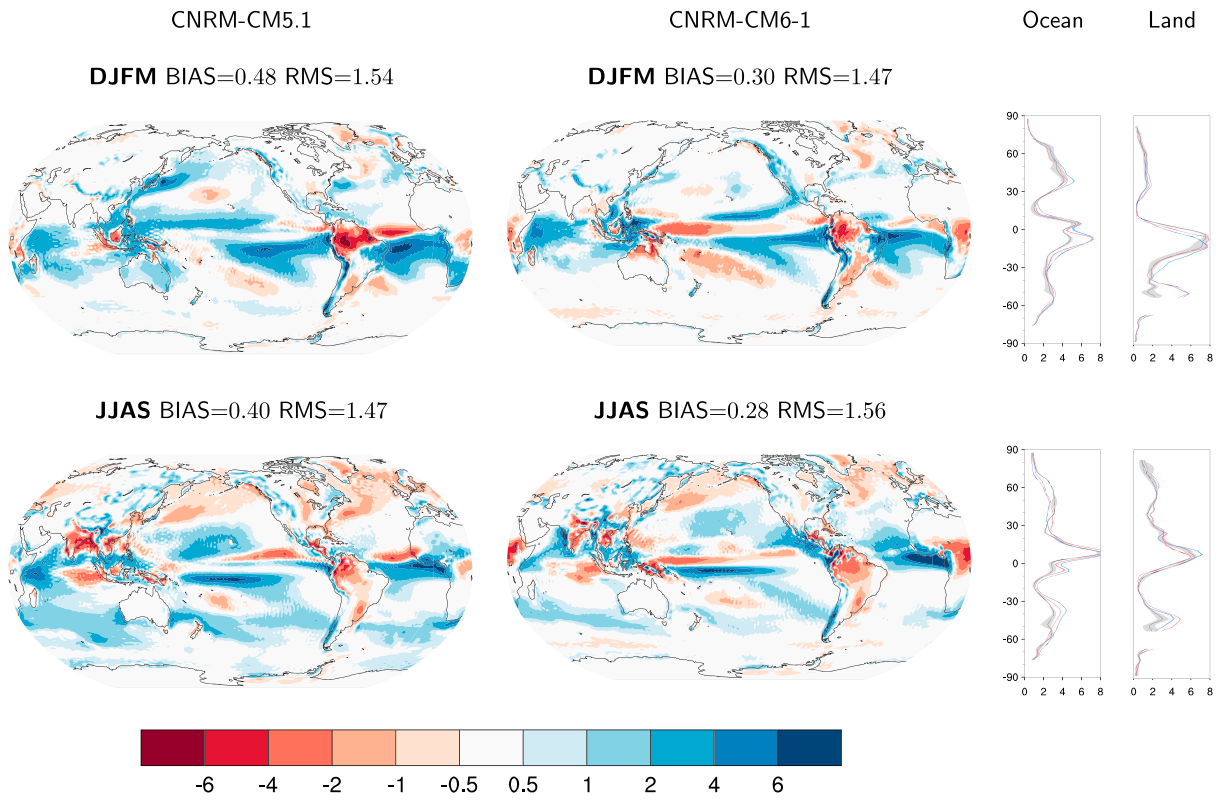

Figure 5. Same as Figure 4 for precipitation but with zonal mean absolute values instead of errors on zonal mean plots. Reference datasets are detailed in Appendix A. DJFM = December–March; JJAS = June–September.

exceed the axis scale on the zonal mean bias figure, for CNRM-CM6-1, the bias is ~8 °C, whereas it reaches 12 °C in CNRM-CM5.1). CNRM-CM6-1 is also warmer over North-Africa, Europe, Scandinavia, and Russia, which mostly constitutes an improvement compared to CNRM-CM5.1, and to a certain extent, compared to most CMIP5 models (Cattiaux et al., 2013; Woods et al., 2017). However, this warming leads to the appearance of a warm bias over Eastern Siberia in CNRM-CM6-1, which is not present in CNRM-CM5.1.

During the boreal summer (June–September), CNRM-CM5.1 has warm biases over the northern hemisphere continents, as most CMIP5 models (Cattiaux et al., 2013; Christensen & Boberg, 2012; Mueller & Seneviratne, 2014). This systematic bias has been significantly reduced in CNRM-CM6-1, and it has almost disappeared in Eastern Europe, Ukraine, and North America's great plains. This improvement is attributed to the soil moisture scheme and to the aerosol-cloud scheme changes. Indeed, changes in ISBA physics from a simple bucket force-restore scheme, as used in CNRM-CM5.1, to a multilayer diffusive soil combined with the representation of groundwater upward capillarity fluxes and floodplain infiltration, as used in CNRM-CM6-1, lead to a larger simulated soil moisture and to increase the seasonal memory of the system that favors summer evaporation (Decharme et al., 2019). Beyond the soil scheme improvements, there is also an atmospheric source of improvement, as pictured on figure 6, there is a net increase in cloud shortwave radiation effect over northern hemisphere continents. On the contrary, results are deteriorated in Central Africa where CNRM-CM6-1 presents a warm bias which is consistent with the precipitation dry bias (Figure 5).

As for the surface temperature, the mean precipitation field exhibits biases of similar amplitude and sometimes spatial patterns between the two CNRM-CM versions (Figure 5). The main differences lie in the western tropical Pacific where CNRM-CM6-1 has now a dry bias, and in Central and West Africa where, for instance, CNRM-CM6-1 partly missed the summertime West African monsoon. On the opposite, the Indian monsoon rainfall pattern is significantly improved and the June–September precipitation excess in the Southern Ocean is largely reduced. The daily distribution of precipitation is also much improved, most probably in relationship with the major update of the convection scheme (not shown). In CNRM-CM5.1, the occurrence of light precipitation events was largely overestimated to the detriment of the frequency of dry

Table 2
Global Mean Radiative Quantities Estimated From CERES Data (2000–2015) and in Both Model Versions on the Period 1981–2010 Averaged Over 10 Members of Historical Simulations

W/m^2		CERES	CNRM-CM5.1	CNRM-CM6-1
Shortwave	Downard surface radiation	187	189	194
	Clear sky downward surface radiation	244	232	251
	Top of atmosphere outgoing radiation	100	96	102
	Top of the atmosphere outgoing clear sky radiation	52	54	54
Longwave	Downard surface radiation	345	337	334
	Clear sky downward surface radiation	317	312	309
	Top of atmosphere outgoing radiation	240	240	237
	Top of the atmosphere outgoing clear sky radiation	266	262	259

Note. CERES = Clouds and the Earth's Radiant Energy System.

days. The frequency of moderate to heavy rainfalls was also overestimated, while extreme precipitation were not frequent enough. CNRM-CM6.1 is much more realistic throughout the spectrum of daily precipitation, both over land and ocean.

With regard to the global-mean radiative budget, the strongest differences between CNRM-CM5.1 and CNRM-CM6.1 concern the clear-sky SW surface radiation and upward SW radiation at the top of the atmosphere (Table 2). The first one is probably due the update of aerosols optical properties in CNRM-CM6-1. The second one might also be due to these aerosols properties changes but is more likely related to the cloud cover increase which also increases the planetary albedo. In both cases, these differences make the model closer to the Clouds and the Earth's Radiant Energy System (CERES) reference data set. In addition, the cooling SW cloud radiative effect (CRE) is increased in CNRM-CM6-1 in the midlatitudes, where it results in a reduced bias (Figure 6), whereas in the (oceanic and continental) convection and trade cumulus tropical regions, it remains overestimated. Over the eastern part of tropical ocean basins, SW CRE biases are reduced, consistently with reduced SST biases, except over the North Pacific where the new atmospheric model has a

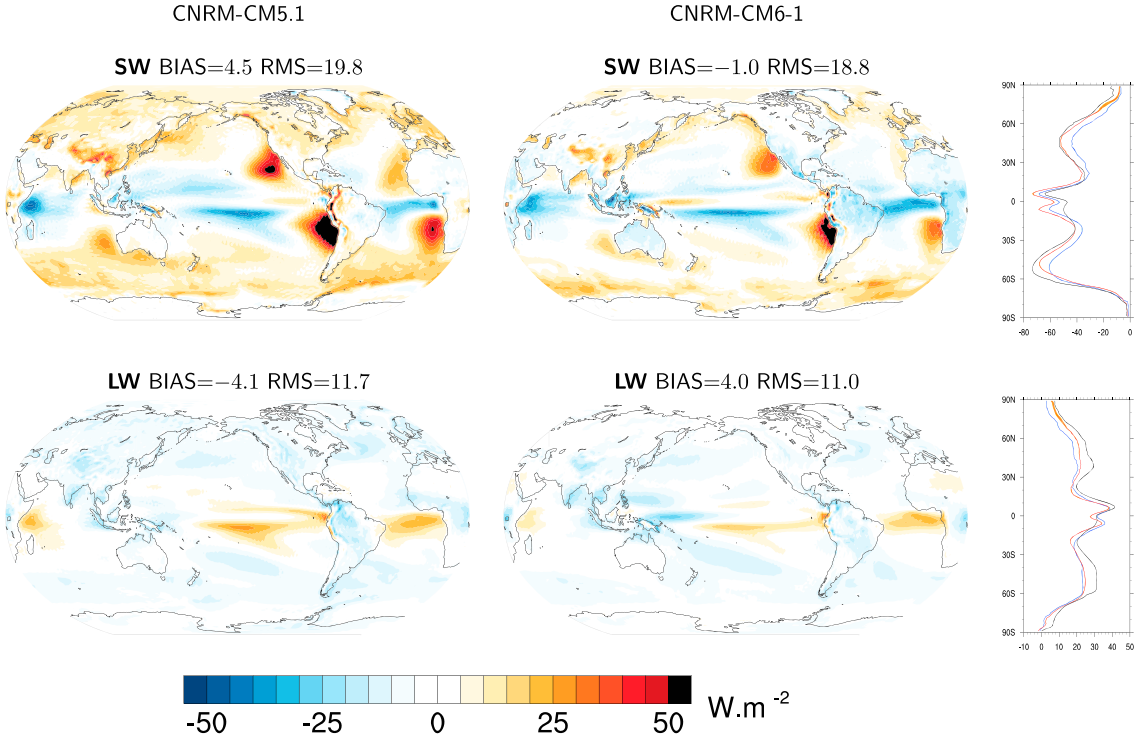

Figure 6. Annual averaged cloud radiative effect bias (W/m^2) in shortwave (SW; top) and longwave (LW; bottom) in CNRM-CM5.1 (left) and CNRM-CM6-1 (middle) historical simulations (1981–2010) compared to Clouds and the Earth's Radiant Energy System (CERES; 2000–2014) and (right) zonal mean prole of cloud radiative effect for CERES (black) and model simulations CNRM-CM6-1 (red) and CNRM-CM5.1 (blue).

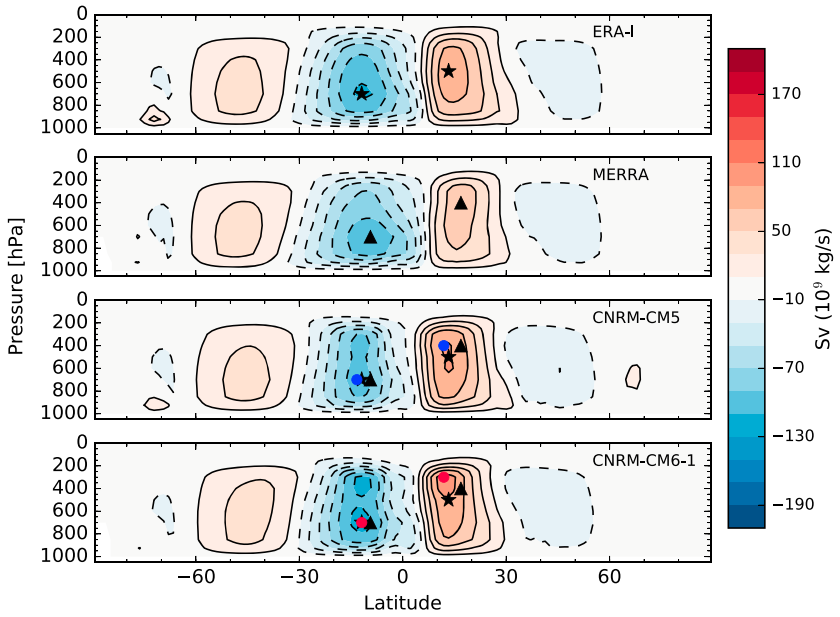

Figure 7. Zonal-mean annual-mean meridional overturning stream functions in isobaric coordinates in ERA-Interim, MERRA, CNRM-CM5.1 and CNRM-CM6-1 during 1981–2010. Positive values represent clockwise circulation and negative values represent anticlockwise circulation. The maximum and minimum of the stream functions are shown as black markers for ERA-Interim and MERRA and as blue dot for CNRM-CM5.1 and red dot for CNRM-CM6-1.

persistent warm bias. For LW radiation, CNRM-CM6-1 global mean fluxes are slightly lower than in CNRM-CM5.1 (Table 2). The LW CRE is weakly changed from a zonal mean perspective, but regional biases are generally reduced compared to CNRM-CM5.1.

The Hadley circulation plays a major role by redistributing momentum and heat from the tropics to higher latitudes. Figure 7 shows the annual climatology of meridional mass stream function, computed from the zonal-mean meridional wind for two reanalyses, ERA-Interim (Dee et al., 2014) and MERRA (Rienecker et al., 2011), and for CNRM-CM5.1 and CNRM-CM6-1 model simulations. In ERA-Interim, the annual Hadley cell is stronger than in MERRA, with the largest difference being in the ascending branch, which is consistent with the findings of Nguyen et al. (2013), who show that MERRA reanalysis produces one of the weakest meridional circulation.

The spatial structure of the mass stream function derived from CNRM-CM6-1 historical simulations and the two reanalyses are consistent with a southern cell higher than the northern cell. The extension of the southern cell at 5°–10°N is also well captured, and the descending branches of the two cells are located at about 30°S and 30°N.

The location and the amplitude of the mass stream function maximum value, commonly used as an index to measure the overturning strength, are close to thoses in the reanalyses in the southern hemisphere. In the northern one, the Hadley cell is stronger, both in CNRM-CM5.1 and CNRM-CM6-1 models. The maximum is located at higher altitudes in CNRM-CM6-1. However, other reanalyses (e.g., National Centers for Environmental Prediction (NCEP) and JRA) also produced a higher circulation center (Stachnik & Schumacher, 2011). During boreal winter and summer (not shown), the Hadley cells simulated by CNRM-CM6-1 also exhibit a higher localization and a larger amplitude of the stream function maximum value, but the biases remain within the range of uncertainties among reanalyses.

Given the major update made on atmospheric parameterizations, the surface mean climate state variable are reasonably simulated.

4.2. Land

Many changes have also been done on the hydrological core of the ISBA-CTRIP land surface system in CNRM-CM6-1. Today, the Gravity Recovery and Climate Experiment (GRACE) gravity products

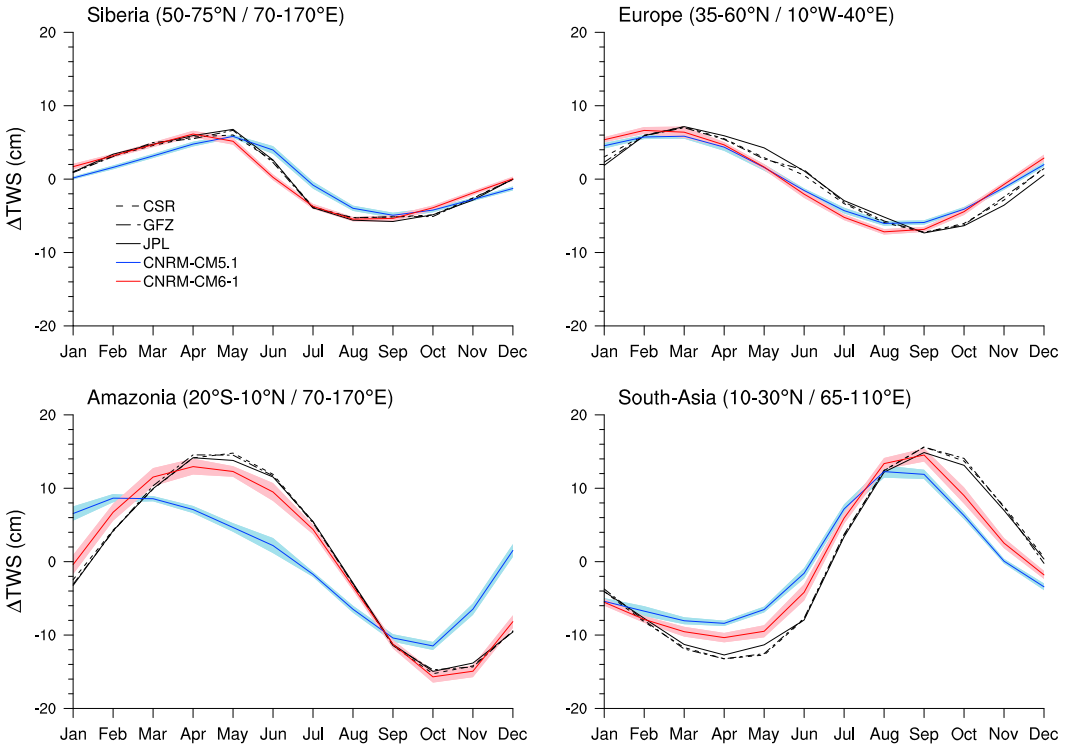

Figure 8. Comparison between observed and simulated monthly mean seasonal cycles of Terrestrial Water Storage time variations over Siberia, Europe, Amazonia, and South Asia. Observations are in black, CNRM-CM5.1 in blue, and CNRM-CM6-1 in red; shading shows the inter-member range for each model (±1,64 times the inter-member variance). Details on observation products and processing can be found in Appendix A. CSR = Center for Space Research; GFZ = GeoForschungsZentrum; JPL = Jet Propulsion Laboratory.

(Swenson, 2012) estimate all changes in continental water masses through the time variations in terrestrial water storage (ΔTWS). In CNRM-CM5.1, ΔTWS is comparable to the sum of time variations in snowpack, canopy water, total soil moisture (including soil ice), and river water mass, while in CNRM-CM6-1 floodplains and groundwater storage are added. Figure 8 compares the ΔTWS mean annual cycle simulated by CNRM-CM5.1 and CNRM-CM6-1 to GRACE estimates over four regions: Siberia, Europe, Amazonia, and South Asia. Improvements are clearly seen over the tropics and, to a lesser extent, over the northern high latitudes. As shown in Decharme et al. (2019), over Amazonia, this result is attributable both to the new diffusive soil scheme in ISBA and the new groundwater and floodplain schemes in CTRIP. These increase the memory of the system in CNRM-CM6-1 and shift the simulated maximum ΔTWS toward that estimated by GRACE. Over Siberia, the better annual cycle simulated by CNRM-CM6-1 is due to the use of a variable river streamflow velocity in CTRIP (Decharme et al., 2010) rather than to an improvement in the representation of snow processes (in CNRM-CM5.1, this velocity was constant and equal to 0.5 m/s).

The snow is an active component of the climate system, especially over northern high-latitude regions where a drastic decrease in springtime snow cover over recent decades (Derksen & Brown, 2012) contributes to the polar warming amplification (Holland & Bitz, 2003). In addition, the snowpack controls the temperature of the soil and then the possible carbon emissions due to the permafrost thawing (e.g., Schuur et al., 2015). A good simulation of both the northern Arctic snow and surface albedo is thus required in climate models to address scientific questions in these regions. Many efforts have thus been made these last years to improve theirs representations in CNRM-CM6-1. The mean annual cycles of snow and surface albedo simulated by CNRM-CM6-1 are clearly more realistic than in CNRM-CM5.1 (Figure 9). These results can be directly related to a better representation of snow processes and snow albedo in the new snow scheme (Decharme et al., 2016) used in CNRM-CM6-1, while the appropriate albedo value during summer is more due to the use of the Moderate Resolution Imaging Spectroradiometer albedo for the land surface.

The reader is referred to Decharme et al. (2019) for a more comprehensive evaluation of the land component.

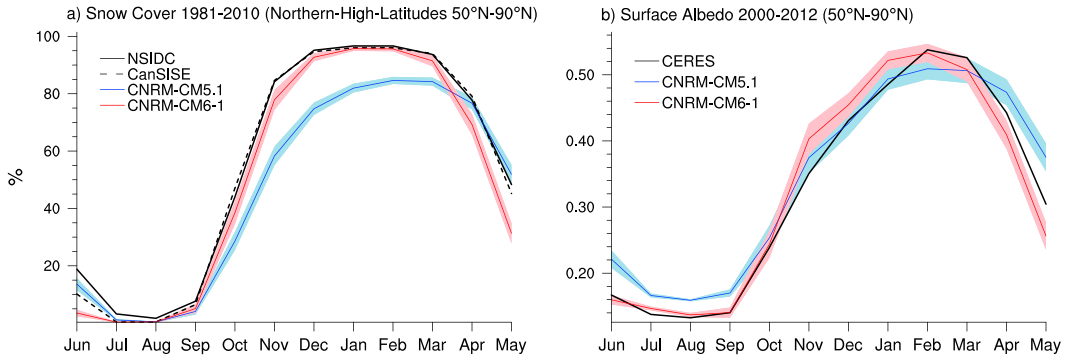

Figure 9. Comparison between observed and simulated monthly mean seasonal cycles of (a) snow cover extents and (b) surface albedo. Observations are in black, CNRM-CM5.1 in blue and CNRM-CM6-1 in red; shading shows the inter-member range for each model (±1,64 times the inter-member variance). Details on observation products and processing can be found in Appendix A. NSIDC = National Snow and Ice Data Center; CERES = Clouds and the Earth's Radiant Energy System.

4.3. Ocean

Overall, the ocean temperature bias is smaller in CNRM-CM6-1 than in CNRM-CM5.1 in all basins (Figure 10). In the Atlantic, a cold bias persists in CNRM-CM6-1 in the northern midlatitudes but the near surface bias is much smaller than in CNRM-CM5.1, probably in part because of the higher ocean vertical resolution. As already noted on SST, the CNRM-CM5.1 strong warm bias in the Southern Ocean is largely reduced in CNRM-CM6-1 and this improvement is also clear at depth. A warm bias persists in CNRM-CM6-1 between 300- and 1,000-m depth from 30°S to 30°N, but it is much smaller than in CNRM-CM5.1, indicating a better representation of the Antarctic intermediate water masses.

CNRM-CM6-1 shows saltier North Atlantic waters than observed at high latitudes, (Figure 11) consistent with the strong deep convection simulated in the Gin Seas (Figure 12). In the Pacific and Indian basins, the temperature bias is quite similar between the two models, albeit smaller at high latitudes in CNRM-CM6-1. The salinity bias in the Pacific is more hemispheric in CNRM-CM6-1 with water masses that are too salty in the Northern Hemisphere and too fresh in the Southern Hemisphere. The fact that this bias is present from the surface to about 300 m suggests that it could be related to an atmosphere bias in net surface water flux.

Figure 12 displays the annual maximum mixed layer depth as modeled by CNRM-CM5.1 and CNRM-CM6-1 and observed from ARGO measurements (Holte et al., 2017). The main observed deep convection areas are located in the Labrador Sea and the Greenland—Iceland—Nordic Seas. They are reasonably well reproduced in both model versions, although with a predominant deep convection in the latter region for CNRM-CM6-1.

For the Southern Hemisphere, there is no deep convection observed during the ARGO period, but it has been documented in the past over the Weddell Sea (Gordon, 1982) and Ross Sea (Jacobs et al., 1970). CNRM-CM5.1 displays weak deep convection in the Weddell Sea, whereas CNRM-CM6-1 has a semipermanent polynia in the Indian sector of the Southern Ocean. This explains relatively larger root-mean-square errors (RMSEs) in the newer version (151 m compared to 87 m), mean biases being comparable and modest (−9 m compared to +5 m). Opposite to CNRM-CM5.1, CNRM-CM6-1 does not simulate deep convection in the Mediterranean Sea whereas it does in the Japan Sea. Finally, both models simulate intermediate convection at subpolar fronts, with an equatorward bias though.

The mean barotropic circulation is very similar in both model versions (Figure 13). It is slightly more intense in the newer version, which causes lower biases (−2 Sv compared to −5 Sv) and RMSEs (26 Sv compared to 31 Sv) with respect to Colin de Verdière and Ollitrault (2016) climatology. The main circulation features are represented by both versions: subtropical and subpolar gyres and the Antarctic Circumpolar Current. However, they are largely underestimated, mostly because of the unresolved mesoscale dynamics along western boundaries. The Antarctic Circumpolar Current reaches respectively 87 Sv in CNRM-CM5.1 and 108 Sv in CNRM-CM6-1, far weaker than the latest estimations of 170−173 Sv (Colin de Verdière & Ollitrault, 2016;

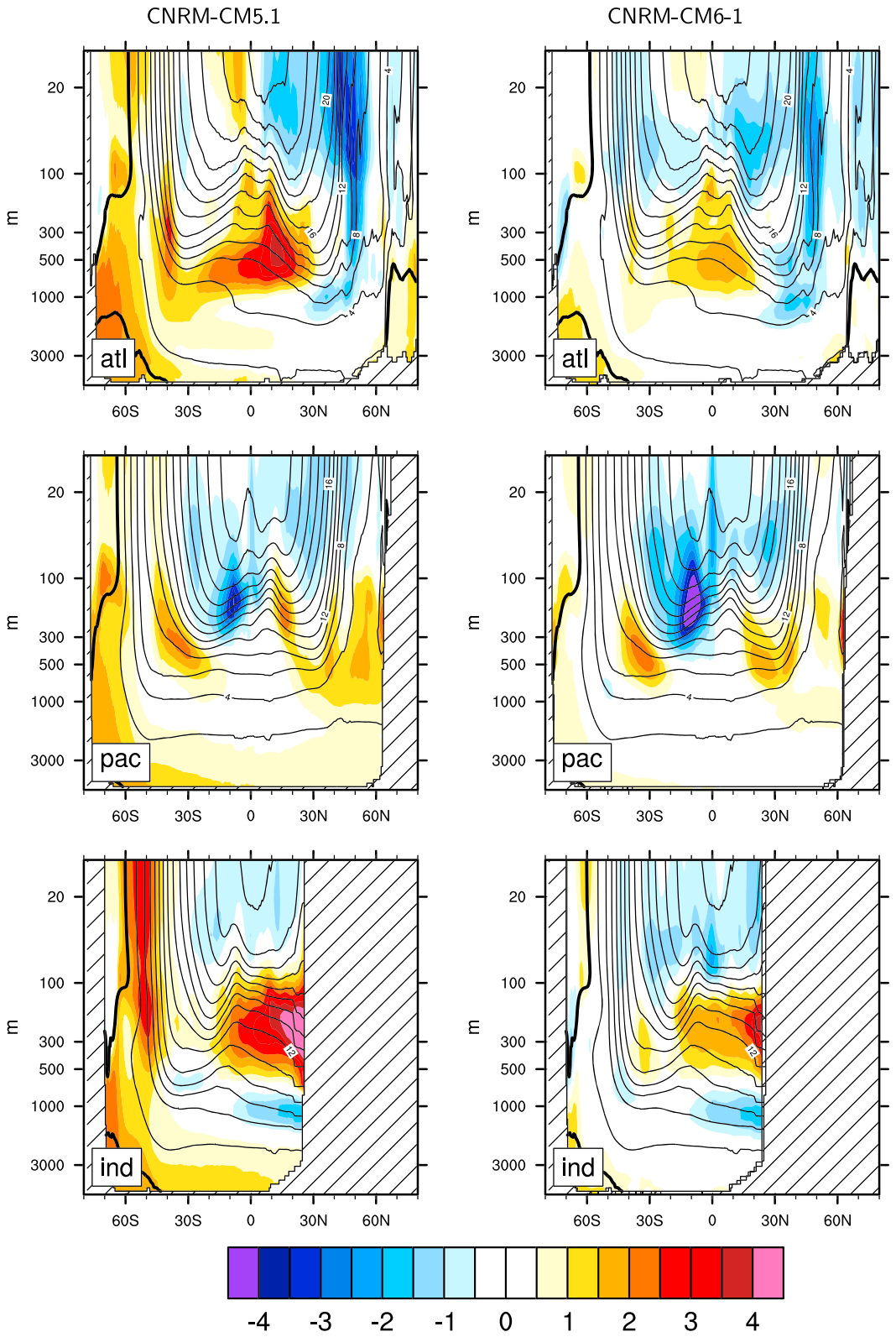

Figure 10. Zonal mean potential temperature bias (shading) in °C in CNRM-CM5.1 (left column) CNRM-CM6-1 (right column) in the Atlantic (top row), Pacific (middle row), and Indian basins (bottom row). The observed climatology from the World Ocean Atlas (WOA) is shown in contours. A logarithmic scale has been applied to the vertical coordinate (depth) to allow a better visualization.

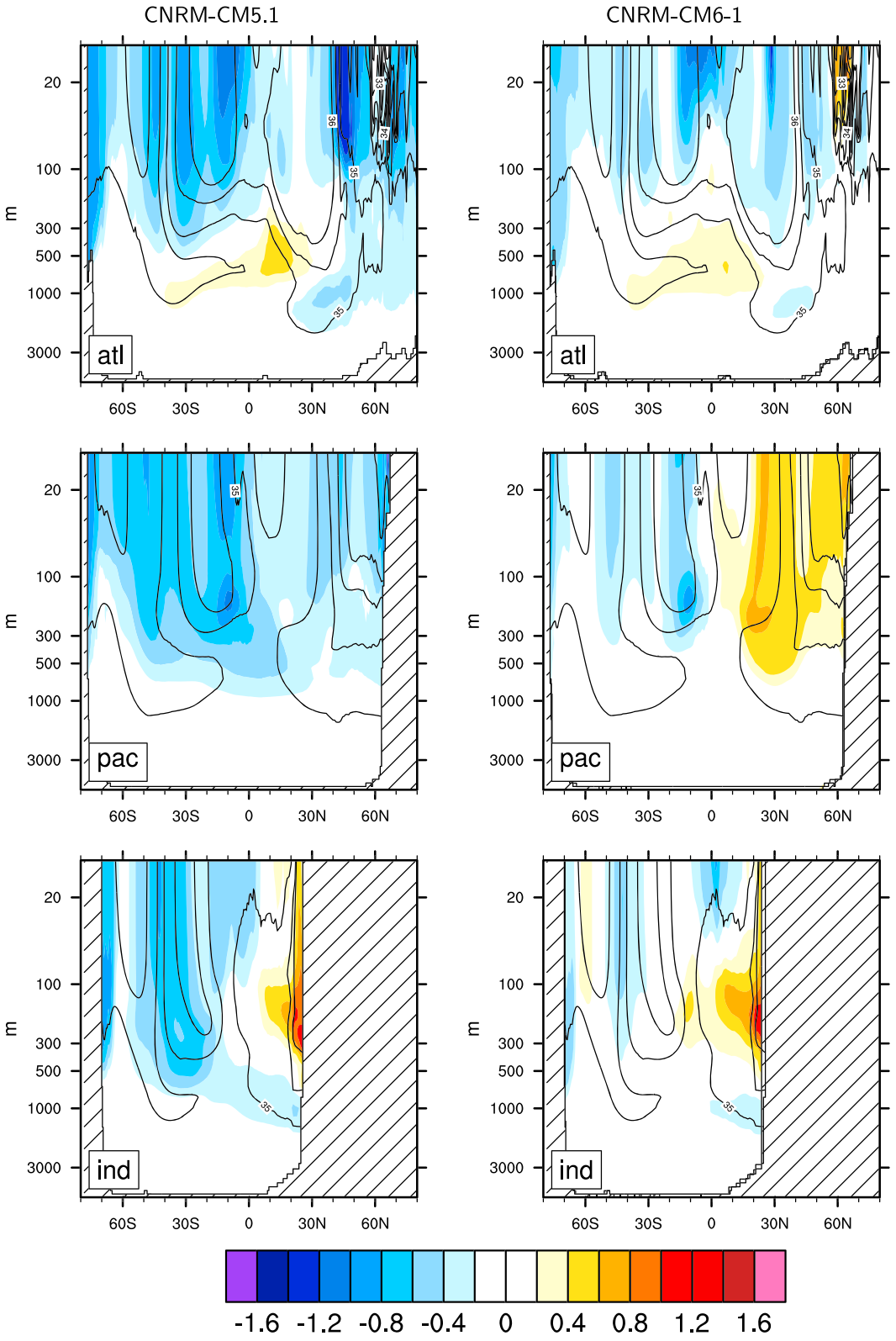

Figure 11. Same as Figure 10 for salinity in psu.

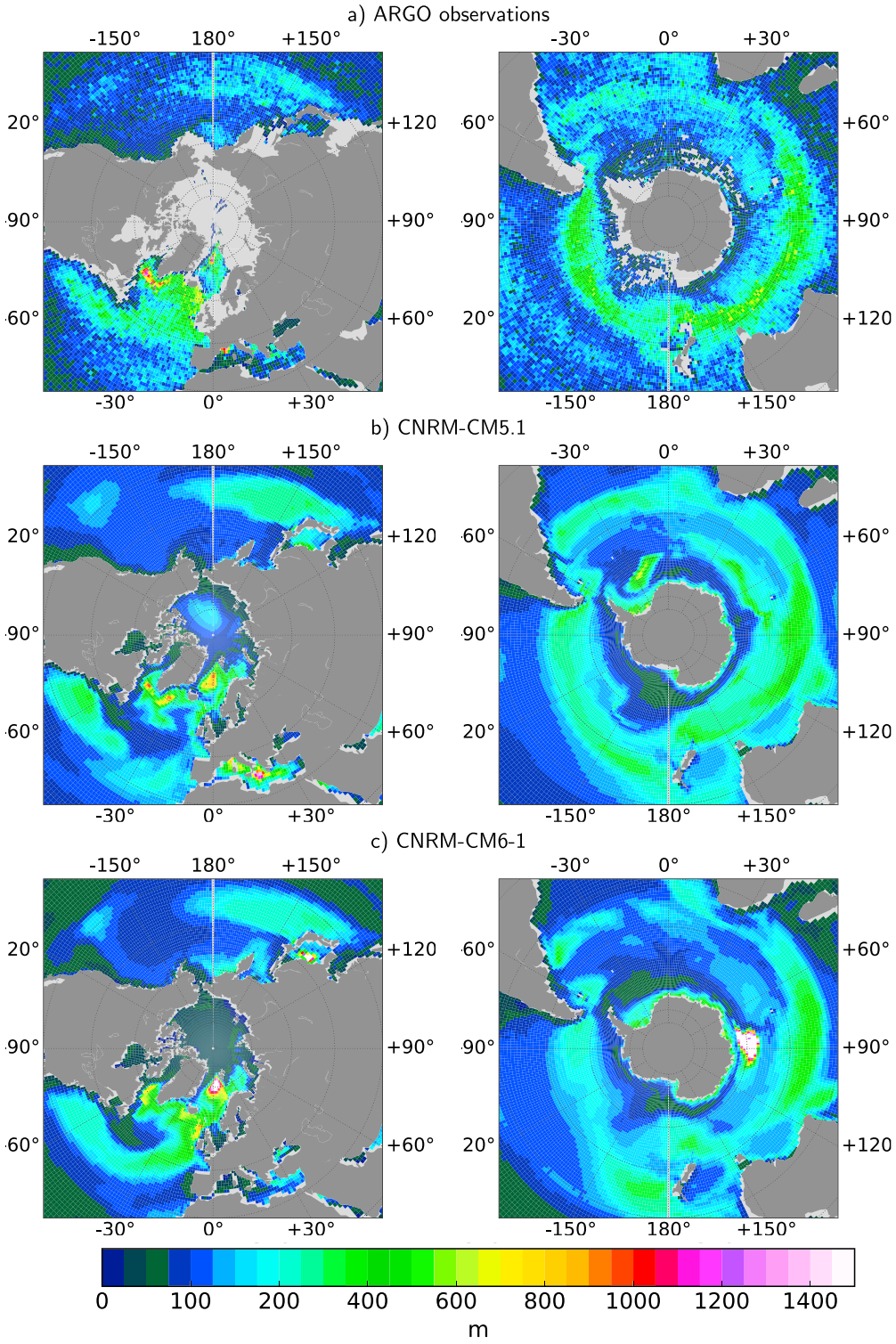

Figure 12. Annual maximum mixed layer depth (a) reconstructed from the 2004–2018 ARGO observations (Holte et al., 2017), averaged over the 1981–2010 period of the ensemble mean historical for (b) CNRM-CM5.1 and (c) CNRM-CM6-1. The mixed layer maximum is computed from monthly means. In models, it is defined with the density threshold of $\rho = 0.03$ kg/m^3 with respect to density at 10 m, and in Holte et al. (2017) climatology it follows the definition from de Boyer Montégut et al. (2004).

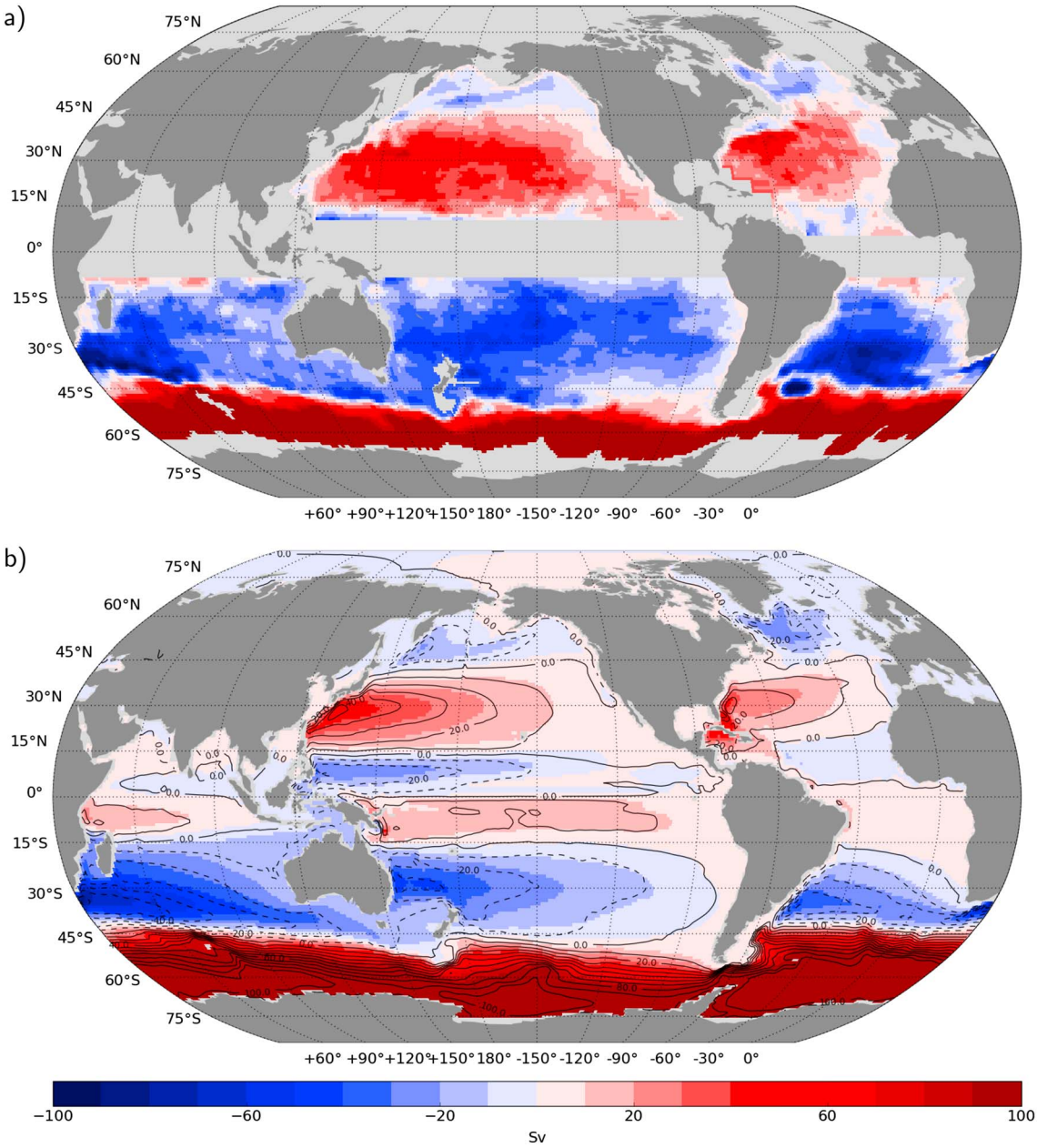

Figure 13. (a) Barotropic stream function reconstructed from the World Ocean Atlas 2009 climatology and mean ARGO float drifts (Colin de Verdière & Ollitrault, 2016) and (b) 1981–2010 mean ocean barotropic stream function from CNRM-CM6-1 (shades) and CNRM-CM5.1 (contours) ensemble mean historical simulations (in Sv). In models, the reference null value is taken over the African-Eurasian continents.

Donohue et al., 2016). Finally, consistently with mixed layer biases, the separation between subtropical and subpolar gyres associated with the subpolar front is too equatorward in both models, especially in the Northern Hemisphere.

The mean Atlantic Meridional Overturning Circulation (AMOC) in CNRM-CM6-1 is much stronger than in CNRM-CM5.1 with a maximum of about 18 Sv located around 35°N and 1,000-m depth, while in CNRM-CM5.1 the maximum was 14 Sv at 26°N and about 800 m (Figure 14). The North Atlantic Deep Water (NADW) cell is deeper in CNRM-CM6-1, which contributes to the reduced temperature and salinity biases (Figures 10 and 11). The maximum value of the ensemble mean MOC profile at 26°N (Figure 14c) is very close to the observed value (~17 versus 18 Sv, McCarthy et al., 2017) although it occurs shallower than observed (800 m instead of 1,100 m). Overall, the ensemble mean profile in CNRM-CM6-1 is very close to

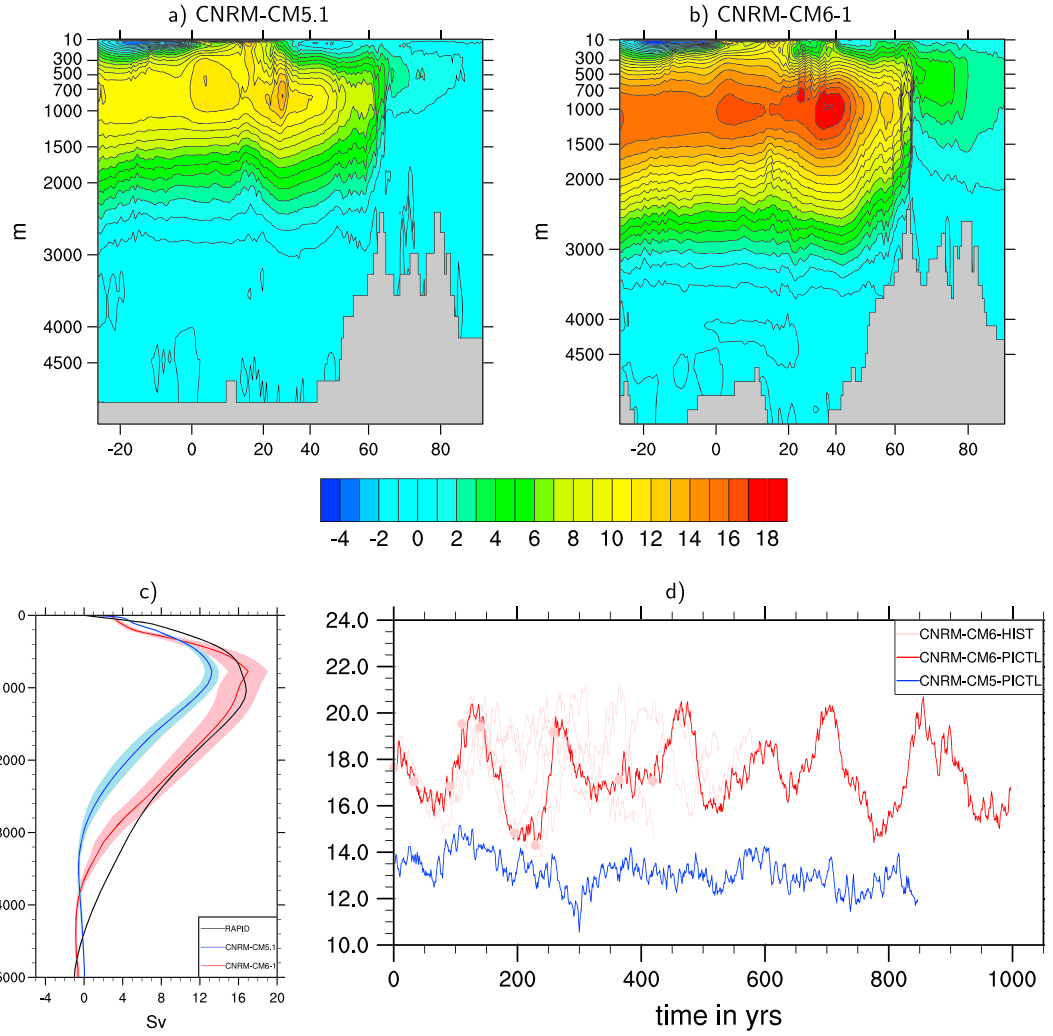

Figure 14. Mean Atlantic Meridional Overturning Circulation (AMOC; in Sv) in the CNRM-CM5.1 (a) and CNRM-CM6-1 (b) model averaged over the 10 historical members over the period 1981–2010. Vertical profile (c) of the mean (1981–2010) MOC at 26°N (d) in CNRM-CM5.1 (blue), CNRM-CM6-1 (red) and in RAPID observations (black). The plain line corresponds to the 10 historical mean and the shading to the inter-member spread. The period used for RAPID is April 2004 to February 2017. All the data have been interpolated on the CNRM-CM6-1 vertical grid. AMOC index (d) defined by the annual value of the stream function maximum at 26°N in CNRM-CM6-1 (red) and in CNRM-CM5.1 (blue) preindustrial simulations. The AMOC time series of the 10 historical simulations of CNRM-CM6-1 are shown in pink. A 5-year running mean have been applied to all time series.

observations in the upper 2,500 m indicating a good representation of the upper NADW cell. The lower NADW cell is too shallow as shown by the return flow that occurs around 3,500 m compared to 4,500 m in observations. The spread in CNRM-CM6-1 is larger than in CNRM-CM5.1. This large spread is due to a marked multidecadal and centennial variability in the Atlantic in CNRM-CM6-1 as shown by the fluctuations of the AMOC at 26°N (Figure 14d). The AMOC peak-to-peak variations are much larger than in CNRM-CM5.1 and the period of the oscillations is around 200 years whereas it was closer to 100 years in CNRM-CM5.1 (Ruprich-Robert & Cassou, 2015). The mechanisms behind this low-frequency Atlantic variability in CNRM-CM6-1 are still under investigation. Preliminary analysis suggests a possible link with freshwater exchanges in the Arctic.

While the atmosphere is the dominant contributor to the total meridional transport (Trenberth & Caron, 2001), biases in the ocean transport have to be compensated for by the atmosphere and can therefore lead to discrepancies in the whole coupled system. It is thus important to assess the fidelity of the climate simulations in representing the meridional transport by the ocean. The global ocean heat transport shown in

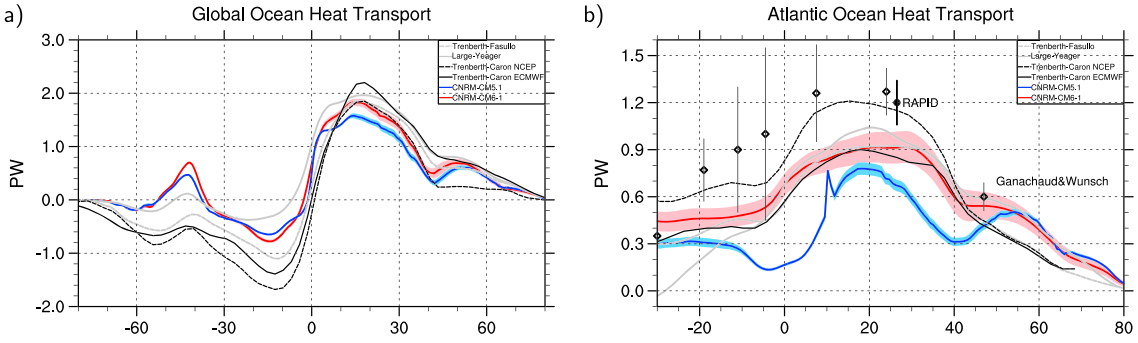

Figure 15. (a) Global and (b) Atlantic ocean heat transport simulated in CNRM-CM6-1 (red) and CNRM-CM5.1 (blue) and in different observational estimates (black and gray, see Appendix A for references). Ten historical simulations are considered for the models with the thick plain line corresponding to the ensemble mean and the shading indicating the spread (estimated by ±1,64 times the inter-member variance). For the Atlantic, only two members are considered for CNRM-CM5.1 because the necessary data were not available for other members.

Figure 15a indicates that more heat is transported northward in CNRM-CM6-1 than in CNRM-CM5.1 in the Northern Hemisphere. The intensity of the peak around 15°N is closer to observational estimates. In the southern midlatitudes, both models show an equatorward transport, which is in agreement with the observation estimate by Large and Yeager (2009) but in disagreement with most other estimates that suggest a poleward transport. The Southern Hemisphere ocean transport was pointed out to be a problematic aspect of many CMIP5 simulations and reanalysis. This highlights the marked difficulties in representing the large-scale energy processes in the Southern Ocean as discussed by Trenberth and Fasullo (2010).

The mean Atlantic Ocean heat transport shows a marked improvement in CNRM-CM6-1 compared to CNRM-CM5.1, at all latitudes. The maximum transport is located around 25°–30°N, in agreement with observations. It peaks at a value of about 0.9 PW, which remains below the observational estimates of RAPID (Johns et al., 2011), Ganachaud and Wunsch (2003), and Trenberth and Caron (2001) but is about 20% larger than the transport simulated by CNRM-CM5.1 around that latitude. This increased meridional transport can be partly explained by the larger overturning heat transport in CNRM-CM6-1, which results for the stronger AMOC at the latitude of the maximum transport (Figure 14).

4.4. Sea Ice

The ensemble mean bias of panarctic sea ice extent simulated by CNRM-CM6-1 with respect to National Snow and Ice Data Center (NSIDC) observations (Fetterer et al., 2017) is close to zero from June to November (Figure 16a), in improvement compared to CNRM-CM5.1. During the rest of the year, the bias is slightly positive (up to 1.2 × 10^6km^2 in May) and slightly reduced compared to CNRM-CM5.1. The

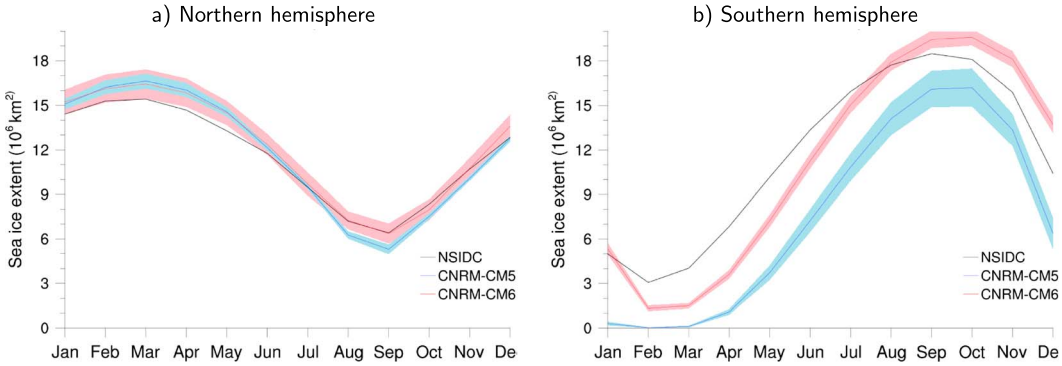

Figure 16. Sea ice extent (in 10^6 km^2) mean annual cycles for 1981–2010 for the Northern (a) and Southern (b) hemisphere, respectively. Satellite observations (Fetterer et al., 2017) are represented by the black thick curve. The sea ice extent annual cycles simulated by CNRM-CM6-1 and CNRM-CM5.1 are respectively depicted by the red and blue curves. The pink and light blue shaded areas represent the 10-member ensemble spread (±1,95 times the inter-member variance) respectively for CNRM-CM6-1 and CNRM-CM5.1.

RMSE of sea ice extent as simulated by CNRM-CM6-1, at $0.7 \times 10^6 km^2$, is slightly reduced compared to CNRM-CM5.1 ($0.9 \times 10^6 km^2$), and the ensemble spread is more pronounced than for CNRM-CM5.1.

The geographic distribution of sea ice simulated by CNRM-CM6-1 in the Arctic is overall realistic, even if a slight eastward shift of the winter ice edge can be seen in the Norwegian Sea compared to CNRM-CM5.1 and observations (Figures 17a–17c). In September, the ice edge in the Beaufort Sea is better positioned than in CNRM-CM5.1. The origin of the bias in CNRM-CM5.1 was found to arise mainly from dynamic causes due to the displacement of the Beaufort Sea high compared to observations, causing surface wind and sea ice transport biases. The reduction of local sea level pressure biases in CNRM-CM6-1 and the updated sea ice dynamics contribute to the improvement of the simulated position of the ice edge.

The observed sea ice thickness gradient between North Greenland and North Siberia is not represented in CNRM-CM6-1. The simulated sea ice was too thin in September and March in CNRM-CM5.1 compared with GIOMAS reconstructions (Zhang & Rothrock, 2003) and is even thinner in CNRM-CM6-1 (Figures 17a–17f). All atmospheric and oceanic forcing fields were analyzed in order to understand this underestimation. Biases in annual mean radiative heat fluxes and turbulent heat exchanges between sea ice and the atmosphere are smaller in CNRM-CM6-1 than in CNRM-CM5.1, but the net atmospheric heat flux is similar. The annual mean ocean-sea ice sensible heat flux is weaker in CNRM-CM6-1 than in CNRM-CM5.1; thus, we could expect less sea ice melting from the bottom. The main difference between the two versions of the model is the much thicker snow layer on sea ice in CNRM-CM6-1. In winter, the thickness of the snowpack is about 0.50 m, which is overestimated compared with the more realistic 0.30 m simulated in CNRM-CM5.1. This thick snow layer has thus an excessive insulating effect on sea ice that limits its growth in CNRM-CM6-1 in winter. In summer, contrary to observations, the snow pack does not melt away completely in CNRM-CM6-1, whereas it did in CNRM-CM5.1. The associated increased albedo leads to an underestimation of the amount of solar short wave radiation absorbed by the snow-ice system in CNRM-CM6-1 and less surface melting.

In the Antarctic, the annual cycle of sea ice extent is better simulated in CNRM-CM6-1 than CNRM-CM5.1, and the ensemble spread is reduced (Figure 16b). The RMSE with respect to the NSIDC satellite retrievals decreases from 4.4 to $2.1 \times 10^6 km^2$. The sea ice cover simulated by CNRM-CM6-1 is too extensive from September to December but not enough from February to June. CNRM-CM5.1 did not simulate any sea ice in March, contrary to observations, whereas the sea ice simulated by CNRM-CM6-1 is more realistic as some sea ice survives the Antarctic summer in the Weddell Sea (Figures 17g–17i). Like in the Arctic, the snowpack is thicker in CNRM-CM6-1 than in CNRM-CM5.1 (not shown). However, in contrast with the Arctic, this results in an increase of sea ice production. In this region, sea ice is thinner than in the Arctic; thus, the ratio snow depth/sea ice depth is higher, which implies that the snow layer is closer to the ocean surface. This promotes the production of snow ice. In CNRM-CM6-1, the position of the ice edge is better simulated in austral winter than in CNRM-CM5.1 in the North East of the Weddell Sea sector and in the Indian sector but does not change much in other regions.

5. Simulated Climate Variability

The CNRM-CM6-1 representation of the mean climate is similar or improved compared to the previous model version. In particular, the ocean mean state is clearly better simulated. Here we assess whether these evolutions have an impact on the model variability at different time scales.

5.1. El Niño–Southern Oscillation

The predominant mode of tropical variability, known as the El Niño–Southern Oscillation (ENSO), is commonly characterized from the Niño-3.4 index computed as the area average of monthly SST anomalies in the region, 5°N–5°S, 170°–120°W. A power spectrum analysis of the Niño-3.4 SST index is shown in Figure 18a for the CNRM-CM5.1 piControl integration, the CNRM-CM6-1 piControl integration, and two observational data sets (ERSSTv5 and HadISST) over 1900–2015. CNRM-CM6-1 exhibits a single sharp spectral peak in the 3- to 4-year band, while observations show a double-peak structure spanning the period range 3.5–8 years. There is a slight improvement compared to CNRM-CM5.1 whose dominant period is too short (2–3.5 year). The maximum power in CNRM-CM6-1 (and CNRM-CM5.1) is similar to observations, although a quantitative comparison would require to integrate the spectra over the appropriate frequency band. We also note

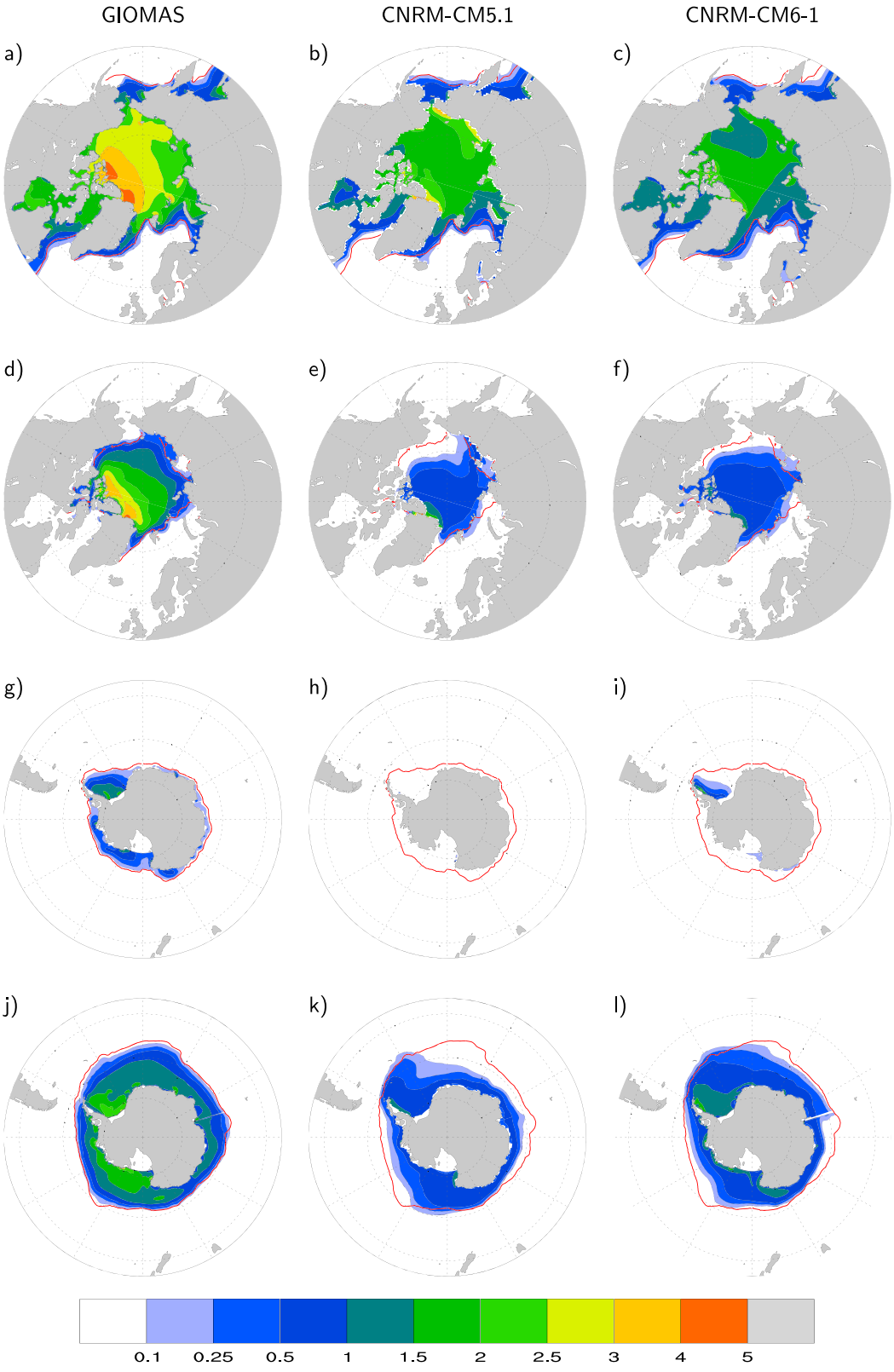

Figure 17. Mean sea ice thickness (m) from GIOMAS (Zhang & Rothrock, 2003; a, d, g, and j) and simulated by CNRM-CM5.1 (b, e, h, and k) and CNRM-CM6-1 (c, f, i, and l) for 1981–2010. The first and second rows are respectively for March and September in the Arctic. The third and fourth rows are for March and September in the Antarctic. The mean sea ice edge, defined here as the 15% sea ice concentration contour line, is inferred from the HadISST data set (Rayner et al., 2003) and is depicted by the thick red lines.

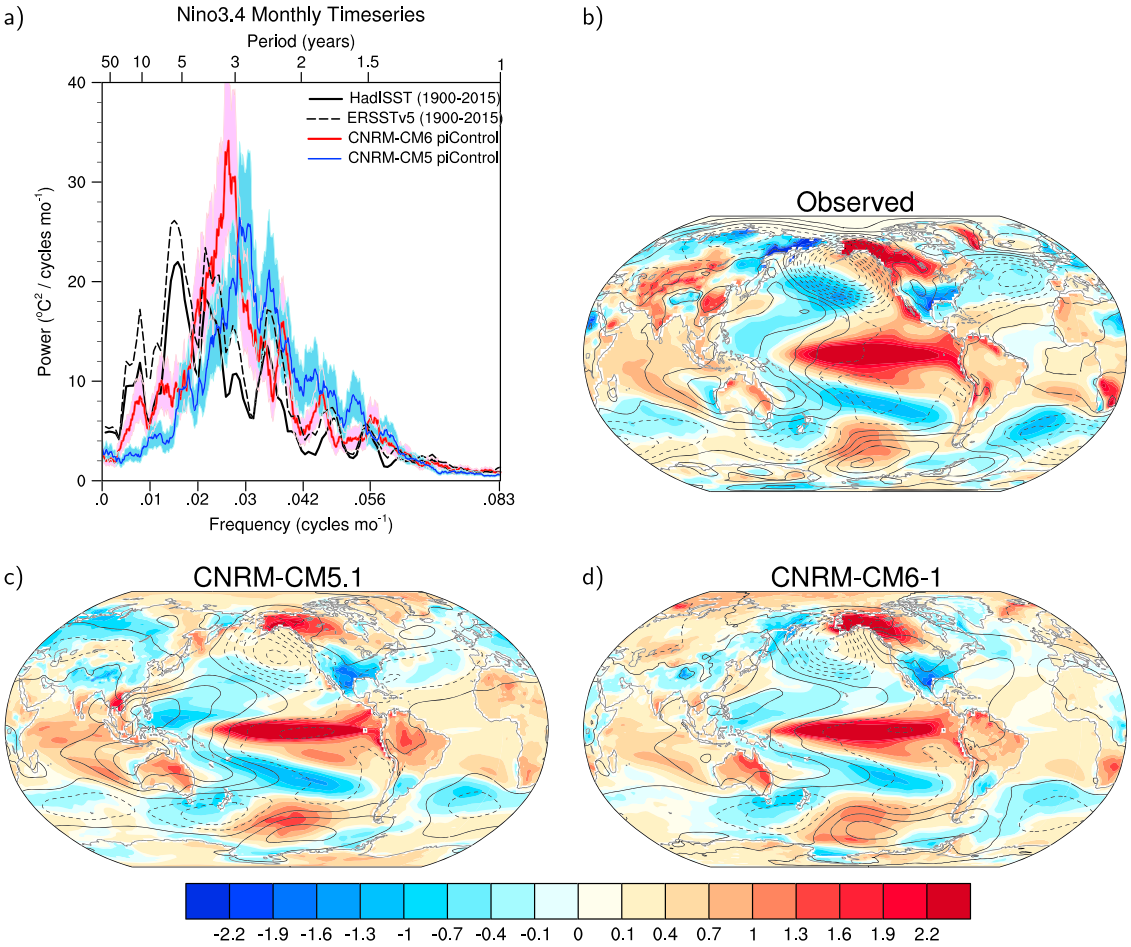

Figure 18. (a) Power spectrum ($°C^2$ (cycles month)$^{-1}$ and period in years) of the Nino-3.4 SST index from detrended observations (ERSSTv5, black dashed curve for 1900–2015 and HadISST, solid black curve for 1900–2015), detrended CNRM-CM6-1 (model years 1850–2849; red curve), and detrended CNRM-CM5.1 (model years 1850–2699; blue curve). The light-red (blue) shading depicts the 5%–95% confidence intervals for the CNRM-CM6-1 (CNRM-CM5.1) spectrum based on the individual spectra for each non-overlapping 100-year segment. (b) El Niño minus La Niña winter (December–February) composite of sea surface temperature (SST) and terrestrial air temperature (°C; shaded) and sea level pressure (contour interval of 1 hPa) for the observations (ERSSTv5 and NCEP), (c) CNRM-CM5.1, and (d) CNRM-CM6-1. Winters with a normalized Niño-3.4 SST index absolute value greater than 1 are used to form the positive and negative composites. The model composites have been scaled to match the observed composite amplitude of the winter Niño-3.4 SST index.

that CNRM-CM6-1 better agrees with observations in the high- and low-frequency parts of the spectrum, albeit CNRM-CM6-1 still underestimates the spectral power at low frequency.

Global teleconnection patterns associated with ENSO are assessed from composite differences between El Niño and La Niña years (Figures 18b–18d; see caption for methodological details). In the observations, the strongest sea level pressure (SLP) response occurs in the Northern Hemisphere, with negative anomalies over the North Pacific and a meridional SLP dipole over the North Atlantic. The former is well captured by both versions of the CNRM model, while the latter is weak in CNRM-CM5.1 and absent in CNRM-CM6-1. Note, however, that the small differences in extratropical teleconnections between model and observations might not be robust given the length of the observational record (Deser et al., 2017). Compared to CNRM-CM5.1, CNRM-CM6-1 better captures the main features of the observed terrestrial air temperature response, including the negative (positive) temperature anomalies over the southeastern United States (western Canada and Alaska) as well as the positive temperature anomalies over South Africa. It also improves the tropical land temperature response, including the Nordeste as well as Western and Eastern Africa. Finally, it is worth noting that as many coupled models, CNRM-CM6-1 (and CNRM-CM5.1) depicts ENSO equatorial Pacific SST anomalies that extend too far west compared to observations.

5.2. Tropical Intraseasonal Variability

Capturing the diversity in the tropical intraseasonal variability, including synoptic disturbances, convectively coupled equatorial waves (i.e., Kelvin, equatorial Rossby, mixed Rossby-gravity, and inertio-gravity waves) and the Madden and Julian Oscillation (MJO, Madden & Julian, 1971; Zhang, 2005), still remains a real challenge for most state-of-the-art climate models (Hung et al., 2013). A common way to diagnose this variability consists in computing the space-time coherence squared and phase lag spectra between the daily averaged outgoing longwave radiation (OLR) and 850-hPa zonal wind (Waliser et al., 2009; Wheeler & Kiladis, 1999), as shown on Figure 19. The method is applied here for both symmetric and antisymmetric components of the two variables (with respect to the equator). The spectra are computed on individual latitudes between 10°S and 10°N and for 120-day time segments overlapping by 100 days, before being averaged (see also Leroux et al., 2016). As a reference, the National Oceanic and Atmospheric Administration Advanced Very High Resolution Radiometer OLR (Liebmann & Smith, 1996) and the ERA-Interim (Dee et al., 2014) 850-hPa zonal wind are used over the period from 1979 to 2008 (Figures 19a and 19b). This reference data set emphasizes the strong coupling between convection and dynamics for Kelvin, equatorial Rossby, eastward inertio-gravity, and mixed Rossby-gravity waves, as well as for the MJO.

For CNRM-CM5.1 (Figures 19c and 19d) and CNRM-CM6-1 (Figures 19e and 19f), one member of historical simulations from 1976 to 2005 is used to estimate the spectra but they do not depend much on the chosen period or member (not shown). CNRM-CM5.1 was known to be one of the few models able to capture a realistic MJO signal (Hung et al., 2013; Figures 19c and 19d). Convectively coupled equatorial waves were however rather poorly simulated, with too fast Kelvin waves, weak equatorial Rossby waves, and almost fully missed mixed-Rossby and eastward inertio-gravity waves. CNRM-CM6-1 shows an overall improvement in that regard (Figures 19e and 19f), even though Kelvin waves do not propagate fast enough and correspond to too small spatial scales. The MJO signal remains, albeit weaker, especially for wave number 1 and higher frequencies. The reasons for this reduction in MJO signal are not fully understood at this stage.

5.3. North Atlantic Oscillation

In the extratropics, the main modes of atmospheric variability at intraseasonal to interannual time scales are referred to as annular modes. In the North-Atlantic region, the Northern Annular Mode (NAM) corresponds to a concurrent modulation in amplitude of both the Azores high and the Icelandic low, also known as the North-Atlantic Oscillation (NAO). In order to evaluate the representation of this mode by the CNRM model, we define the NAO pattern as the North-Atlantic part (90°E–30°W, 20°–90°N) of the NAM pattern, computed as the first empirical orthogonal function of winter (December–March) monthly SLP anomalies over the whole Northern extratropics (20°–90°N). This definition is the same as used in the literature for the evaluation of CMIP3 (Miller et al., 2006) and CMIP5 (Cattiaux & Cassou, 2013) models (see these references for further methodological details). The reference NAM/NAO pattern is derived from ERA-Interim reanalyses over the period 1981–2010 and is similar to http://www.cpc.ncep.noaa.gov/products/precip/CWlink/daily_ao_index/ao.loading.shtml.

Overall, the CNRM-CM6-1 model represents both the location (spatial correlation) and the magnitude (ratio of standard deviations) of the NAO centers of action fairly well (Figure 20). Although based on 30-year subsets, estimates from historical members are close to the 1,000-year piControl experiment, suggesting that both the sampling uncertainty and the externally forced component are rather small. A substantial improvement can be noted from CNRM-CM5.1 concerning the magnitude of the NAO (ratio of standard deviations closer to 1), resulting in a greater—and more realistic—fraction of interannual European temperature variability explained by the NAO (not shown).

5.4. Atlantic Multidecadal Variability

At global scale, the dominant patterns of decadal climate variability are the Atlantic Multidecadal Variability (AMV) and the Pacific Decadal Variability (PDV). Because of short observational records, sparse spatial sampling, and inconsistency in terms of instrumental biases, it is challenging to clearly elucidate the origins of these modes (Cassou et al., 2018, for a review). Therefore, in this paper, we limit the model evaluation to the SST fingerprint of both AMV and PDV.

The traditional AMV index, defined as the 10-year low-pass-filtered annual North Atlantic anomalies averaged over 0°–60°N, is computed in both versions of the model and the spatiotemporal properties of the

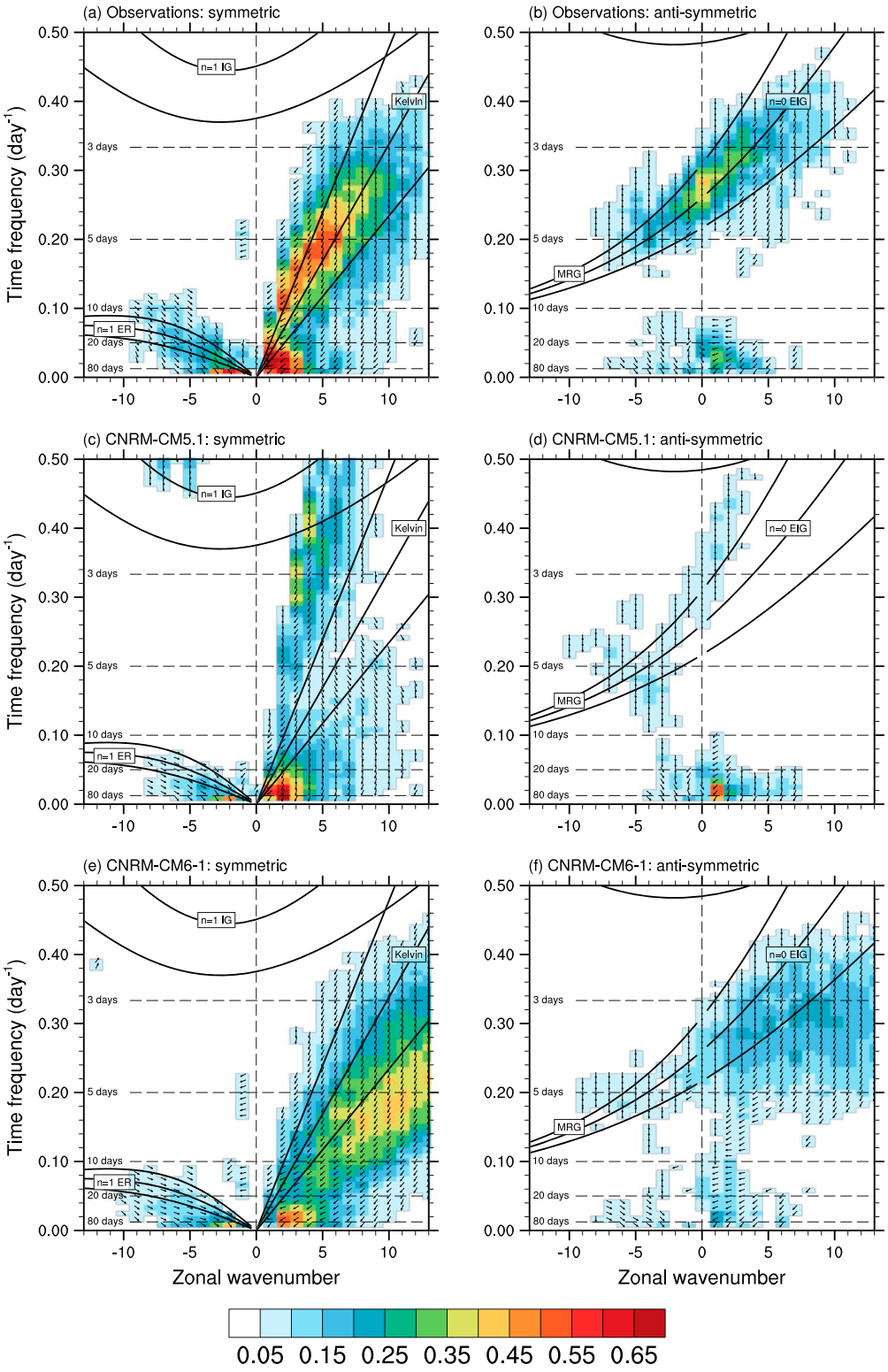

Figure 19. Coherence squared (colors) and phase lag (vectors) between outgoing longwave radiation and 850-hPa zonal wind. Here is shown on panels (a), (c), and (e) the symmetric spectrum and on panels (b), (d), and (f) the antisymmetric spectrum for the reference dataset (National Oceanic and Atmospheric Administration Advanced Very High Resolution Radiometer outgoing longwave radiation and ERA-Interim wind) (a and b), CNRM-CM5.1 (c and d), and CNRM-CM6-1 (e and f). A phase of 0 is represented by a vector directed upward. Dispersion curves for the ($n = -1$) Kelvin, $n = 1$ equatorial Rossby (ER), $n = 1$ inertio-gravity (IG), $n = 0$ eastward intertio-gravity (EIG), mixed Rossbygravity (MRG) modes corresponding to three equivalent depths ($h = 12$, 25, and 50 m) in the shallow water equations are overlaid (black lines). See text for further details.

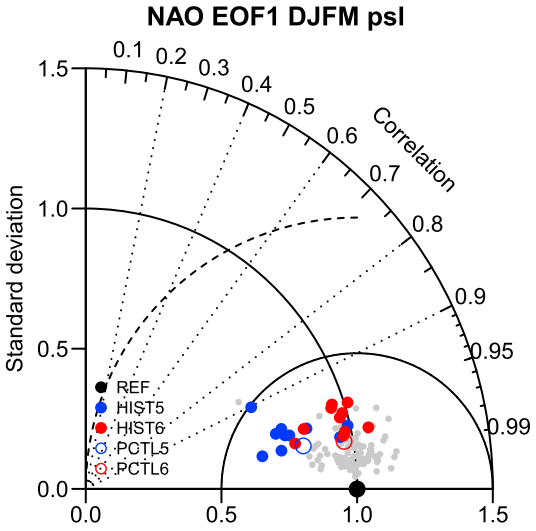

Figure 20. Taylor diagram summarizing the representation of the North Atlantic Oscillation (NAO) pattern by the CNRM model. NAO is defined as the first empirical orthogonal function (EOF) of December–March (DJFM) sea level pressure anomalies. The reference pattern is taken from ERA-Interim over 1981–2010. Ratio of standard deviation (radial distance), spatial correlation (radial angle) and resulting root-mean-square errors (dashed isolines) are indicated. Blue is CNRM-CM5.1, red is CNRM-CM6-1. Circles are piControl experiments (1,000 years); filled circles are historical members (1981–2010). Gray dots obtained by bootstrapping years of the reference data (ERA-Interim) are intended to illustrate the sampling uncertainty.

simulated AMV are presented in Figure 21. Observational counterpart is provided after removal of the SST externally forced component estimated from optimal filtering (Ting et al., 2009), in compliance with CMIP6 so-called DCPP-C experiments (Boer et al., 2016) aiming at better understanding the teleconnectivity associated with the AMV (Ruprich-Robert et al., 2017).

Power spectrum analysis of the AMV index exhibits a sharp and intense spectral peak around 140 years in CNRM-CM6-1 in contrast to CNRM-CM5.1 which has a much weaker variability at this time scale (Figure 21a). Maximum SST related anomalies are found in the eastern part of the subpolar gyre and in the Nordic Seas; these are indicative for altered oceanic circulation/thermohaline transports and sea ice extent (Figure 21d). A similar spatial pattern was found in CNRM-CM5.1 but with considerably reduced intensity (Figure 21c). Changes in magnitude between the two model versions clearly stand out in the AMV time series (Figure 21e). While the amplitude of decadal variability is rather similar between the two versions, the multidecadal/centennial fluctuations are much stronger in CNRM-CM6.1. The total variance of the AMV index is 0.09 °C in CNRM-CM5.1, which is similar to most of the CMIP5 models but lower than the observations (0,14 °C, Qasmi et al., 2017). This variance reaches 0.19 °C in CNRM-CM6-1, which would make this model an outlier compared to the CMIP5 ensemble. The short duration of the observational record, however, prevents from assessing which model version is the most realistic.

In terms of mechanisms, this multidecadal/centennial mode is associated with the interplay between the AMOC and the freshwater balance of the Arctic Ocean on one hand and the northward salt transport from the tropical Atlantic on the other hand (e.g., Ruprich-Robert & Cassou, 2015). The correlation between the AMV and AMOC is equal to 0.91 both in CNRM-CM6-1 and CNRM-CM5.1. Furthermore, the anomalous SST spatial patterns of both versions (Figures 21c and 21d) resemble the observations despite some underestimation of the AMV-related anomalies in the tropical North Atlantic (Figure 21b). It is worth recalling that the connection between AMOC variations and tropical Atlantic SSTs remains ambiguous in the observations and the mechanisms producing tropical Atlantic SST decadal variability still remain elusive (Cassou et al., 2018).

5.5. Pacific Decadal Variability

PDV is defined here as the leading empirical orthogonal function of annual mean SST over the entire Pacific (limited at the southern edge to 35°S) after removing the externally forced estimate, again following recommendations for the DCPP-C coordinated experiments (Boer et al., 2016, their Figure 7). The PDV index exhibits a maximum loading in a broad spectral band between 10 and 24 years in CNRM-CM6-1 (Figure 22a). CNRM-CM5.1 tends to have a redder behavior despite two distinct peaks of variability around 14 and 18 years. Both modeled anomalous SST patterns (Figures 22c and 2d) bear some resemblance with observations (Figure 22b), albeit with smaller amplitude. The pan-ocean properties of the mode are different in CNRM-CM6-1 compared to CNRM-CM5.1, with maximum amplitude found in the tropics in the former but in the northern extratropical basin in the latter. In both cases, this may be indicative of an underestimated teleconnection with ENSO at decadal timescale. This potential flaw has been highlighted in CNRM-CM5.1 by Nidheesh et al. (2017), and no clear improvement is noted here in CNRM-CM6-1, despite the SST fingerprints of the model flaws are different.

6. Response to External Forcings

6.1. Historical Tendencies

Historical trend in GSAT is well consistent with observations (Figure 23a). The 1995–2014 period as simulated by CNRM-CM6-1 is 0.76 °C warmer than 1850–1900 after applying the observational mask, as compared to +0.75 °C in the HadCRUT4 record. The remarkably large internal variability is easily discernible

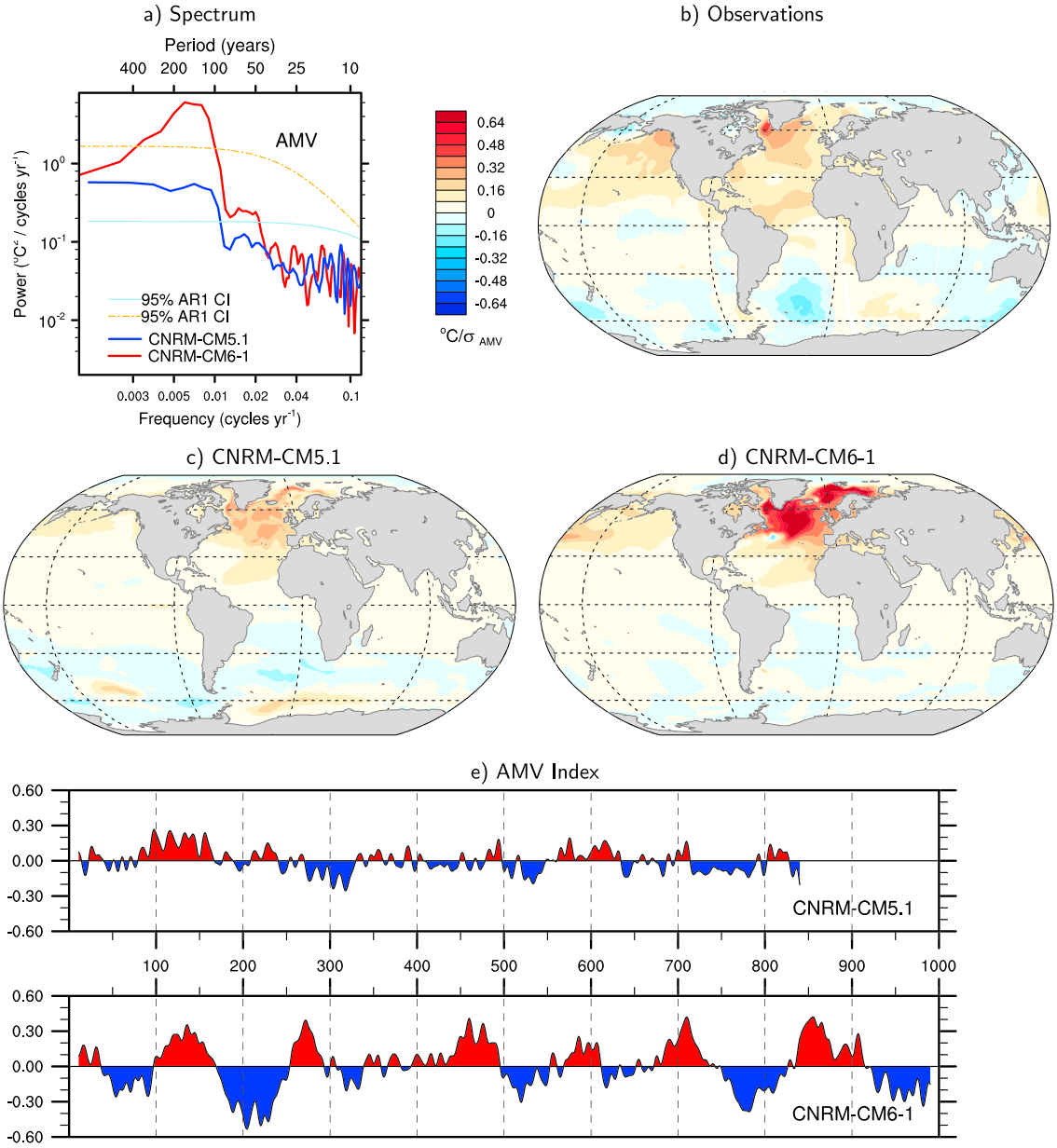

Figure 21. (a) Power spectrum (°C as a function of (cycles year)$^{-1}$ and period in years) of the Atlantic Multidecadal Variability (AMV) sea surface temperature index from detrended CNRM-CM6-1 (red solid line) and CNRM-CM5.1 (blue solid line). Dashed orange and cyan curves stand for the upper confidence bounds at 95% for the two models, respectively. Sea surface temperature regression maps on the AMV index for (b) the observations (ERSSTv5), (c) CNRM-CM5.1, and (d) CNRM-CM6-1. Shading interval for maps is equal to 0.05 °C per standard deviation of the respective AMV indices displayed in (e) for the models (unit is °C).

in the historical ensemble, as the evolution of GSAT over time differs substantially among individual members. Note that anomalies are plotted relative to the 1981–2010 period; thus, spread is artificially removed over this period. The impact of major volcanic eruptions (marked as vertical gray lines) is much less in CNRM-CM6-1 than in CNRM-CM5. This can be attributed both to the change in forcing AOD (Figure 2) and to the improved stratosphere representation mainly due to the increase in vertical levels number.

Concerning late summer Arctic sea ice, its sensitivity in extent seems underestimated (Figure 23b). This underestimation may result from the insulation effect of the thick snow layer on sea ice. The insulating effect limits the production of sea ice and also its melting. The sea ice cover appears as under sensitive in this model.

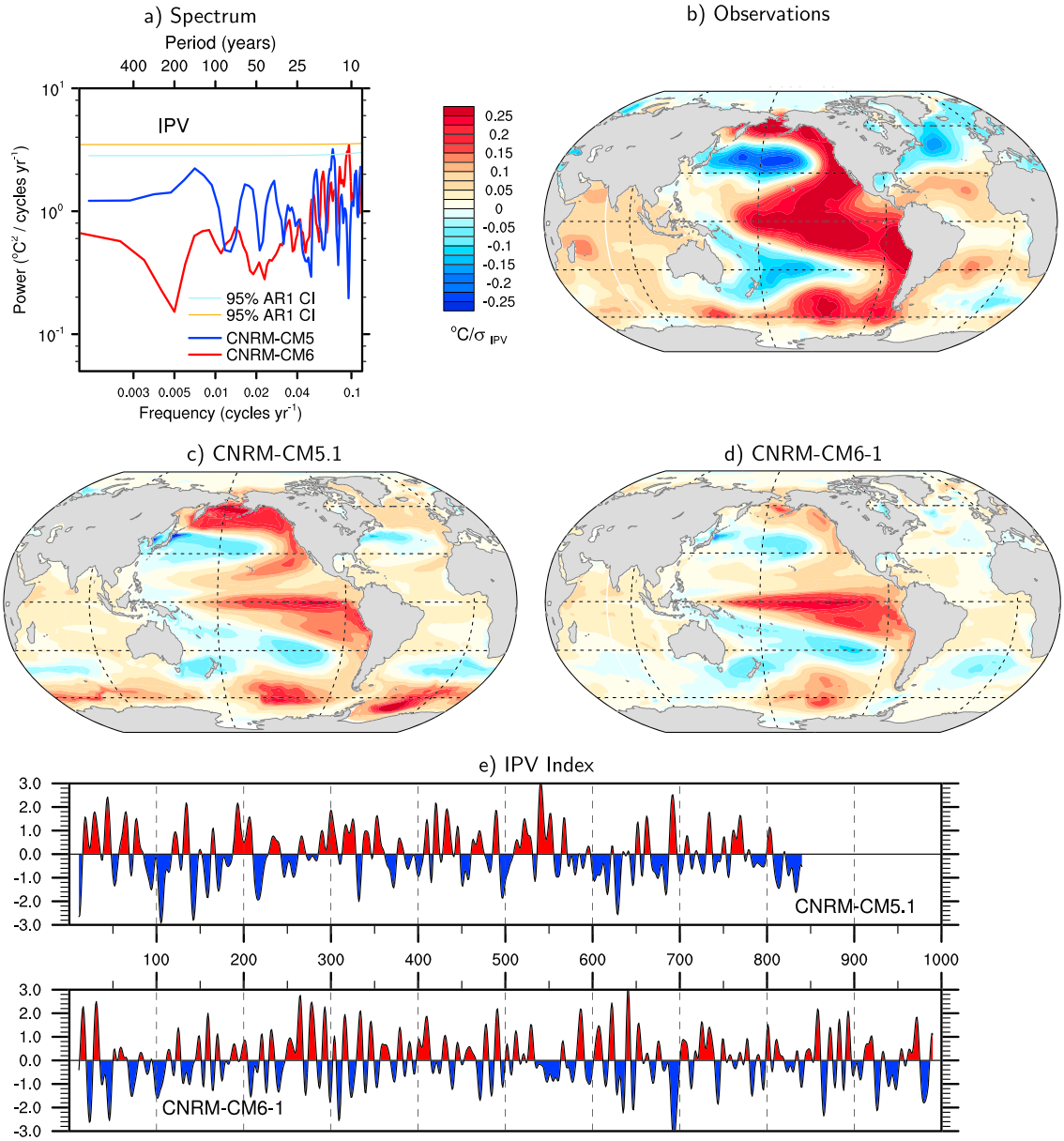

Figure 22. (a) Power spectrum (unitless a function of (cycles year)$^{-1}$ and period in years) of the unfiltered Pacific Decadal Variability (PDV) sea surface temperature index for CNRM-CM6-1 (red solid line) and CNRM-CM5.1 (blue solid line). Dashed orange and cyan curves stand for the upper confidence bounds at 95% for the two models, respectively. Sea surface temperature regression maps on the 10-year low-pass PDV index for (b) the observations (ERSSTv5), (c) CNRM-CM5.1, and (d) CNRM-CM6-1. Shading interval for maps is equal to 0.025 °C per standard deviation of the respective PDV indices displayed in (e) for the models.

Concerning the continental snow, the Fifth Assessment Report of the Intergovernmental Panel on Climate Change report (Stocker et al., 2013) points out a very high confidence that the extent of Northern Hemisphere snow cover has decreased in March and April by approximately 1.6% per decade between 1967 and 2012. This tendency seems to be well reproduced by CNRM-CM6-1 (as well as by CNRM-CM5-1) increasing our confidence that the model is able to represent the long-term evolution of snow processes accurately, at least across the Northern Hemisphere.

6.2. Climate Sensitivity

By using the Gregory et al. (2004) regression method applied to the abrupt 4xCO2 experiment (and rescaling results by a factor 0.5 to compute a 2xCO2 estimate), the effective equilibrium climate sensitivity (ECS) is

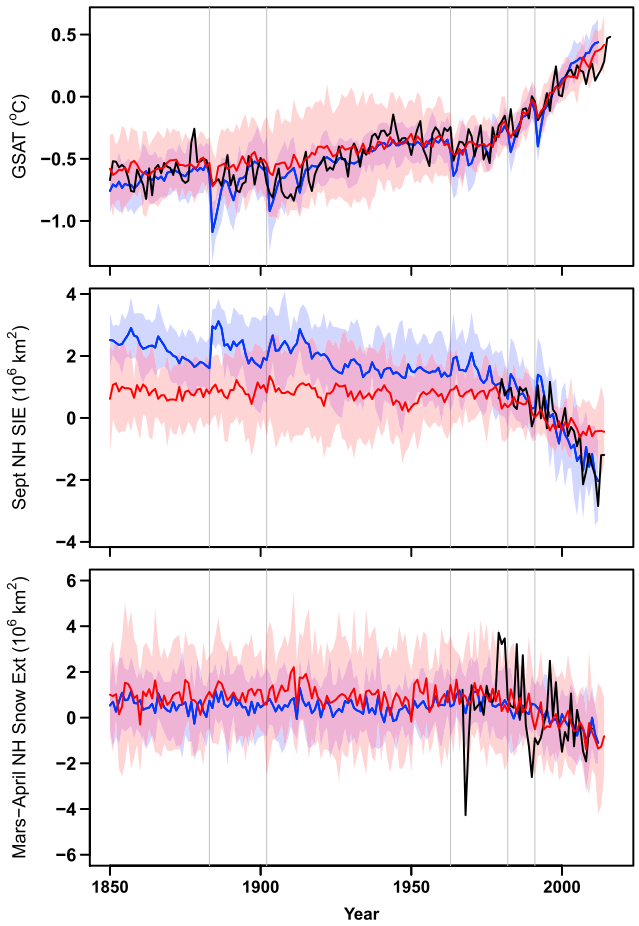

Figure 23. Historical trends in global surface atmospheric temperature (GSAT, top, °C), September sea ice extent in the Northern Hemisphere (middle, 10^6 km^2) and March–April snow cover in the Northern Hemisphere (bottom, 10^6 km^2). Observations in black (see Appendix A for reference data sets) are compared to CNRM-CM5.1 (blue) and CNRM-CM6-1 (red), including ensemble means (thick lines) and inter-member spread (±1,64 times the inter-member variance). All values are anomalies with respect to the 1981–2010 average. Major volcanic eruptions are indicated with gray vertical bars.

equal to 4.9 K. This lies in the upper bound of climate sensitivities projected by CMIP5 climate models (Flato et al., 2013) and is well above the CNRM-CM5.1 ECS (3.3 K). Given the important changes made in the atmospheric component, we would not have expected to obtain the same ECS as in the former model version. In particular, it now better represents low clouds and shallow convection, which are key processes in climate feedbacks (e.g., Sherwood et al., 2014).

The transient climate response (TCR) is estimated to 2 K by using the 10 first years of the 1% CO2 y-1 experiment as a reference, following Flato et al. (2013). While the ECS strongly increased from CNRM-CM5.1 to CNRM-CM6-1, the TCR remains unchanged (2.0 K for CNRM-CM5.1). CNRM-CM5.1 was one of the CMIP5 models with the largest TCR/ECS ratio. The CNRM-CM6-1 ratio is now in the range of CMIP5 estimates. Winton et al. (2014) has shown that this ratio is anti-correlated with the AMOC strength in Geophysical Fluid Dynamics Laboratory Earth system models. Its decrease is thus consistent with the increase of the AMOC strength in CNRM-CM6-1. Consistently with its unchanged TCR, CNRM-CM6-1 simulates a global mean warming still close to historical observations, while having an ECS as large as 4.9 K. This provides a counterexample to several studies showing that observed warming points toward low ECS (e.g., Knutti et al., 2017).

7. Conclusion and Perspectives

In this paper, we have presented the latest version CNRM-CM6-1 of the CNRM-CM suite. Since the CNRM-CM5.1 version used in CMIP5, all components have been upgraded. For ocean, sea ice, and rivers, there was no major change in parameterizations. By contrast, the atmosphere and land surface components have been fully revisited with the use of new state-of-the-art parameterizations. For the atmospheric component, major changes cover the representation of shallow and deep convection, microphysics, and turbulence processes. Over land, the snow and soil schemes have been refined, whereas the hydrology has been enriched to represent river floods and aquifers. The development of coupled climate models suitable for climate change studies and centennial time-scale integrations is known to result from long and subtle efforts in model calibration. As a consequence, given the major updates presented hereabove, the calibration of CNRM-CM6-1 has been a real challenge to achieve a reasonable present-day climate mean state and variability while ensuring energy and water conservation in the system. This can be viewed as replacing compensating errors by more physically based parameterisations. This effort will be pursued to further improve it.

The CNRM-CM6-1 model has been used to perform the CMIP6 DECK experiments and many CMIP6 MIPs, including ScenarioMIP, DAMIP, OMIP, CFMIP, and RFMIP. Files compliant with CMIP6 requirements and straight ready to be published on the Earth System Federated Grid have been produced inline thanks to the use of XIOS, a parallel input/output data server, without any postprocessing step.

Based on a general validation of both the mean climate and variability in DECK experiments, the present paper provides a general picture of CNRM-CM6-1 to the scientific community, which will analyze CMIP6 experiments. Additional papers focusing on individual components performances are under way (see http://www.umr-cnrm.fr/cmip6/references for an updated list). In the course of CNRM-CM6-1 development, one of the main target was to reduce long-term drifts. These are strongly improved in comparison to those in the former CNRM-CM5.1 version. The main improvements highlighted here are a general reduction of ocean biases in temperature and salinity, in particular in the southern ocean where the CNRM-CM5.1 warm bias from the surface to the deeper ocean is much weaker. This is probably linked to the improvement

of shortwave radiative fluxes, which results from both revised aerosols properties and a more realistic cloud cover. Associated to the ocean bias reduction, the simulated AMOC strength and profile are improved in this new model. The representation of land surface hydrology, including snow, also made significant progress in CNRM-CM6-1 (see Decharme et al., 2019, for a more comprehensive assessment).

However, several climate features have little evolved or have even been deteriorated. The African monsoon is now particularly deficient. The sea-ice mean state remains only weakly improved on the Antarctic, while over the Arctic, the insulation by the thick snow layer seems unrealistic. The latter is probably responsible for the slower than observed summer sea-ice retreat in the historical runs. One outstanding result of CNRM-CM5.1 was its capacity to capture several features of the MJO (Hung et al., 2013). CNRM-CM6-1 is less skillful, though still better than many CMIP5 models.

The main modes of interannual to multidecadal variability are reasonably simulated, except for the AMV whose magnitude appears to be overestimated compared to recent observations. This result is consistent with the large low-frequency variability of GSAT and AMOC in the piControl simulation. The reasons for this need to be further investigated.

This large model internal variability has strong implications on the analysis of experiments done with the model. As seen for the historical experiments, the ensemble spread is quite large. We therefore encourage to use as many members as possible to ensure the significance of the analysis performed when using CNRM-CM6-1. Accordingly, we will provide at least 6 members for all Tier 1 ScenarioMIP experiments and 10 members for all Tier 1 DAMIP experiments.

Finally, the equilibrium climate sensitivity of CNRM-CM6-1 is significantly increased compared to that of CNRM-CM5.1. CNRM-CM6-1 now belongs the high sensitivity climate models, at least in the CMIP5 ensemble. At the same time, the transient climate response remains unchanged and the historical warming simulated is compatible with observations.

CNRM-CM6-1 constitutes the physical basis of the CNRM Earth System model, namely, CNRM-ESM-2. CNRM-ESM 2 adds interactive aerosols, stratospheric chemistry, land carbon feedbacks, and ocean biogeochemistry upon CNRM-CM6-1 (http://www.umr-cnrm.fr/cmip6/references). A higher resolution version of CNRM-CM6-1, called CNRM-CM6-1-HR, has also been designed and corresponds to an increase in oceanic resolution to 0.25° and atmospheric resolution to 50 km. This model version is intended to be used to run both the HighResMIP and full DECK experiments.

The assessment made in this paper provides guidelines for future developments of CNRM-CM. In particular, the conservation of mass and energy has been ensured in all components except for energy in the atmosphere. This latter point will be a priority for the next version. The representation of snow on sea ice also needs to be recalibrated to avoid its excessive insulating effect in the Arctic. Specific investigations will also focus on the African monsoon. Further work is also needed to continue the improvement of the representation of cloud cover and both shallow and deep convection.

Appendix A: Observation Products Details

A.1.1. Surface Temperature

Ocean surface temperature biases are assessed against the averaged of HadISST1 (Rayner et al., 2003) and ERSSTv5 (Huang et al., 2017). Land near surface temperature reference is taken as the average of BEST (Muller et al., 2013; Rohde et al., 2013), CRU-TS4-00 (Harris et al., 2014), and GHCN-CAMS (Fan & van den Dool, 2008). Estimation of SST variability modes is also done using the ERSST v5 product.

Historical warming trends are derived from the HadCRUT4 data set, a combination of surface air temperature over land and sea surface temperature (Morice et al., 2012). All data are homogenized, and the observational mask is applied to perform model vs observation comparison.

A.1.2. Precipitation

Precipitation biases are assessed against the average of the following four data set: GPCC (Schneider et al., 2014), GPCP-1.2 (Adler et al., 2003), MSWEP (Beck et al., 2017), and TRMM-L3-4B43-V7 (Huffman et al., 2007).

A.1.3. Cloud Radiative Effect

Cloud radiative effects are compared to the CERES product version "CERES_EBAF_Ed2.8." described in Loeb et al. (2009).

A.1.4. Sea Ice Extent

Satellite Arctic sea ice extent observations are taken from NSIDC sea ice index 3.0 (Fetterer et al., 2017). Model northern hemisphere sea ice extents for September are computed from simulated monthly mean sea ice concentrations, with a threshold value of 15 %.

A.1.5. Snow and Land Surface Albedo

Snow cover extent is given by two data sets. First, the weekly satellite estimates distributed by the NSIDC at 25-km horizontal resolution over the 1966 to 2016 period (Brodzik & Armstrong, 2013) have been remapped at 1° resolution and averaged at a monthly time scale as proposed by Peings et al. (2013). Second, the CanSISE observation-based ensemble of Northern Hemisphere terrestrial SWE version 2 data set at 1° resolution over the 1981 to 2010 period (Mudryk et al., 2018) is used to calculate monthly snow cover extend from the daily time series using a 0.004 kg/m^2 threshold applied to the daily SWE fields as proposed by Mudryk et al. (2017).

Land surface albedo is observed by the Clouds and the Earth's Radiant Energy System (CERES) Energy Balanced and Filled (EBAF) Surface data set Edition 4.0 (Kato et al., 2013; https://ceres.larc.nasa.gov/products.php?product=EBAF-Surface). The CERES EBAF-surface product gives access to monthly surface irradiances at 1° resolution from March 2000 to present. Surface downward and upward shortwave fluxes have been used to derive the land surface albedo over the 2000 to 2012 period.

A.1.6. Terrestrial Water Storage

We used three solutions of monthly ΔTWS estimate from the RL05 GRACE release (Swenson, 2012) provided at 1° resolution by the Center for Space Research at the University of Texas at Austin, the Jet Propulsion Laboratory, and the GeoForschungsZentrum at Potsdam. More details on the data processing and the comparison protocol with model simulations can be found in Landerer and Swenson (2012) and Decharme et al. (2019), respectively.

A.1.7. Ocean Heat Transport

Ocean meridional heat transport estimates from Trenberth and Caron (2001), Large and Yeager (2009) and Trenberth and Fasullo (2010) are considered. Additionally, local estimates by Ganachaud and Wunsch (2003) and on the RAPID transect by Johns et al. (2011) are also indicated.

Acknowledgments
This work has been partially funded by the French ANR project CONVERGENCE under grant ANR-13-MONU-0008-02 and by the H2020 project CRESCENDO "Coordinated Research in Earth Systems and Climate: Experiments, kNowledge, Dissemination and Outreach," which received funding from the European Union's Horizon 2020 research and innovation program under grant agreement 641816. The authors wish to thank Céline Colombo for her work on the model schematic. They also greatly acknowledge the NEMO R&D team for their support in implementing NEMO and its interface with XIOS. We would like to thank Bodeker Scientific, funded by the New Zealand Deep South National Science Challenge, for providing the combined NIWA-BS total column ozone database. The SURFEX-CTRIP code is available (Open-SURFEX) using a CECILL-C Licence (http://www.cecill.info/licences/Licence_CeCILL-C_V1-en.txt) at http://www.umr-cnrm.fr/surfex; the NEMO-GELATO is also available at https://opensource.umr-cnrm.fr/, OASIS3-MCT can be downloaded at https://verc.enes.org/oasis/download, and XIOS can be downloaded at https://forge.ipsl.jussieu.fr/ioserver. For the ARPEGE-Climat v6 code and exact version applied to each component, please contact the authors. CMIP6 CNRM-CM6-1 experiments assessed in this paper are available on the Earth System Grid Federation (ESGF).

References

Adler, R. F., Huffman, G. J., Chang, A., Ferraro, R., Xie, P. P., Janowiak, J., et al. (2003). The version-2 Global Precipitation Climatology Project (GPCP) monthly precipitation analysis (1979–present). *Journal of Hydrometeorology*, *4*(6), 1147–1167. https://doi.org/10.1175/1525-7541(2003)004<1147:TVGPCP>2.0.CO;2

Ammann, C. M., Joos, F., Schimel, D. S., Otto-Bliesner, B. L., & Tomas, R. A. (2007). Solar influence on climate during the past millennium: Results from transient simulations with the NCAR Climate System Model. *Proceedings of the National Academy of Sciences*, *104*(10), 3713–3718. https://doi.org/10.1073/pnas.0605064103

Barnier, B., Madec, G., Penduff, T., Molines, J. M., Treguier, A. M., le Sommer, J., et al. (2009). Impact of partial steps and momentum advection schemes in a global ocean circulation model at eddy-permitting resolution. *Ocean Dynamics*, *59*(3), 537–537. https://doi.org/10.1007/s10236-009-0180-y

Beck, H. E., van Dijk, A. I. J. M., Levizzani, V., Schellekens, J., Miralles, D. G., Martens, B., & de Roo, A. (2017). MSWEP: 3-hourly 0.25° global gridded precipitation (1979–2015) by merging gauge, satellite, and reanalysis data. *Hydrology and Earth System Sciences*, *21*(1), 589–615. https://doi.org/10.5194/hess-21-589-2017

Bermejo, R., & Conde, J. (2002). A conservative quasi-monotone semi-Lagrangian scheme. *Monthly Weather Review*, *130*(2), 423–430. https://doi.org/10.1175/1520-0493(2002)130<0423:ACQMSL>2.0.CO;2

Bodeker, G. E., Shiona, H., & Eskes, H. (2005). Indicators of Antarctic ozone depletion. *Atmospheric Chemistry and Physics*, *5*(10), 2603–2615. https://doi.org/10.5194/acp-5-2603-2005

Boer, G. J., Smith, D. M., Cassou, C., Doblas-Reyes, F., Danabasoglu, G., Kirtman, B., et al. (2016). The Decadal Climate Prediction Project (DCPP) contribution to CMIP6. *Geoscientific Model Development*, *9*(10), 3751–3777. https://doi.org/10.5194/gmd-9-3751-2016

Bougeault, P., & Lacarrère, P. (1989). Parameterization of orography-induced turbulence in a mesobeta-scale model. *Monthly Weather Review*, *117*(8), 1872–1890. https://doi.org/10.1175/1520-0493(1989)117<1872:POOITI>2.0.CO;2

Bouillon, S., Morales Maqueda, M. A., Legat, V., & Fichefet, T. (2009). An elastic-viscous-plastic sea ice model formulated on Arakawa B and C grids. *Ocean Modelling*, *27*(3-4), 174–184. https://doi.org/10.1016/j.ocemod.2009.01.004

Bouteloup, Y., Seity, Y., & Bazile, E. (2011). Description of the sedimentation scheme used operationally in all Météo-France NWP models. *Tellus Series A: Dynamic Meteorology and Oceanography*, *63*(2), 300–311. https://doi.org/10.1111/j.1600-0870.2010.00484.x

Bretherton, C. S., McCaa, J. R., & Grenier, H. (2004). A new parameterization for shallow ccumulus convection and its application to marine subtropical cloud-topped boundary layers. Part I: Description and 1D results. *Monthly Weather Review*, *132*(4), 864–882. https://doi.org/10.1175/1520-0493(2004)132<0864:ANPFSC>2.0.CO;2

Brient, F., Roehrig, R., & Voldoire, A. (2019). Evaluating marine stratocumulus clouds in the CNRM-CM6-1 model using short-term hindcasts. *Journal of Advances in Modeling Earth Systems*, *11*(1), 127–148. https://doi.org/10.1029/2018MS001461

Brodzik MJ, Armstrong R (2013) Northern Hemisphere EASE-Grid 2.0 weekly snow cover and sea ice extent, version 4. Boulder, Colorado USA. NASA Natl Snow Ice Data Cent Distrib Act Arch Cent

Cabré, A., Marinov, I., & Gnanadesikan, A. (2017). Global atmospheric teleconnections and multidecadal climate oscillations driven by Southern Ocean convection. *Journal of Climate*, *30*(20), 8107–8126. https://doi.org/10.1175/JCLI-D-16-0741.1

Cariolle, D., & Teyssèdre, H. (2007). A revised linear ozone photochemistry parameterization for use in transport and general circulation models: multi-annual simulations. *Atmospheric Chemistry and Physics*, *7*(9), 2183–2196. https://doi.org/10.5194/acp-7-2183-2007

Carslaw, K. S., Gordon, H., Hamilton, D. S., Johnson, J. S., Regayre, L. A., Yoshioka, M., & Pringle, K. J. (2017). Aerosols in the pre-industrial atmosphere. *Current Climate Change Reports*, *3*(1), 1–15. https://doi.org/10.1007/s40641-017-0061-2

Cassou, C., Kushnir, Y., Hawkins, E., Pirani, A., Kucharski, F., Kang, I. S., & Caltabiano, N. (2018). Decadal climate variability and predictability: Challenges and opportunities. *Bulletin of the American Meteorological Society*, *99*(3), 479–490. https://doi.org/10.1175/BAMS-D-16-0286.1

Catry, B., Geleyn, J. F., Bouyssel, F., Cedilnik, J., Broková, R., Derková, M., & Richard (2008). A new sub-grid scale lift formulation in a mountain drag parameterisation scheme. *Meteorologische Zeitschrift*, *17*(2), 193–208. https://doi.org/10.1127/0941-2948/2008/0272

Cattiaux, J., & Cassou, C. (2013). Opposite CMIP3/CMIP5 trends in the wintertime Northern Annular Mode explained by combined local sea ice and remote tropical influences. *Geophysical Research Letters*, *40*, 3682–3687. https://doi.org/10.1002/grl.50643

Cattiaux, J., Douville, H., & Peings, Y. (2013). European temperatures in CMIP5: origins of present-day biases and future uncertainties. *Climate Dynamics*, *41*(11-12), 2889–2907. https://doi.org/10.1007/s00382-013-1731-y

Chevallier, M., Salas y Mélia, D., Voldoire, A., Voldoire, A., Déqué, M., & Garric, G. (2013). Seasonal forecasts of the Pan-Arctic sea ice extent using a GCM-based seasonal prediction system. *Journal of Climate*, *26*(16), 6092–6104. https://doi.org/10.1175/jcli-d-12-00612.1

Christensen, J. H., & Boberg, F. (2012). Temperature dependent climate projection deficiencies in CMIP5 models. *Geophysical Research Letters*, *39*, L24705. https://doi.org/10.1029/2012GL053650

Colin de Verdière, A., & Ollitrault, M. (2016). A direct determination of the world ocean barotropic circulation. *Journal of Physical Oceanography*, *46*(1), 255–273. https://doi.org/10.1175/JPO-D-15-0046.1

Craig, A., Valcke, S., & Coquart, L. (2017). Development and performance of a new version of the OASIS coupler, OASIS3-MCT_3.0. *Geoscientific Model Development Discussion*, *10*, 3297–3308. https://doi.org/10.5194/gmd-2017-64

Cuxart, J., Bougeault, P., & Redelsperger, J. L. (2000). A turbulence scheme allowing for mesoscale and large-eddy simulations. *Quarterly Journal of the Royal Meteorological Society*, *126*(562), 1–30. https://doi.org/10.1002/qj.49712656202

Danabasoglu, G., Yeager, S. G., Bailey, D., Behrens, E., Bentsen, M., Bi, D., et al. (2014). North Atlantic simulations in Coordinated Ocean-ice Reference Experiments phase II (CORE-II). Part I: Mean states. *Ocean Model*, *73*, 76–107. https://doi.org/10.1016/j.ocemod.2013.10.005

de Boyer Montégut, C., Madec, G., Fischer, A. S., Lazar, A., & Iudicone, D. (2004). Mixed layer depth over the global ocean: An examination of profile data and a profile-based climatology. *Journal of Geophysical Research*, *109*(C12), C12003. https://doi.org/10.1029/2004JC002378

de Lavergne, C., Falahat, S., Madec, G., Roquet, F., Nycander, J., & Vic, C. (2019). Toward global maps of internal tide energy sinks. *Ocean Model*, *137*, 52–75. https://doi.org/10.1016/J.OCEMOD.2019.03.010

de Lavergne, C., Madec, G., Le Sommer, J., George Nurser, A. J., & Naveira Garabato, A. C. (2016). The impact of a variable mixing efficiency on the abyssal overturning. *Journal of Physical Oceanography*, *46*(2), 663–681. https://doi.org/10.1175/JPO-D-14-0259.1

Decharme, B., Alkama, R., Douville, H., Becker, M., & Cazenave, A. (2010). Global evaluation of the ISBA-TRIP continental hydrological system. Part II: Uncertainties in river routing simulation related to flow velocity and groundwater storage. *Journal of Hydrometeorology*, *11*(3), 601–617. https://doi.org/10.1175/2010JHM1212.1

Decharme, B., Brun, E., Boone, A., Delire, C., le Moigne, P., & Morin, S. (2016). Impacts of snow and organic soils parameterization on northern Eurasian soil temperature profiles simulated by the ISBA land surface model. *The Cryosphere*, *10*(2), 853–877. https://doi.org/10.5194/tc-10-853-2016

Decharme, B., Delire, C., Minvielle, M., Colin, J., Vergnes, J. P., Alias, A., et al. (2019). Recent changes in the ISBA-CTRIP land surface system for use in the CNRM-CM6 climate model and in global off-line hydrological applications. *Journal of Advances in Modeling Earth Systems*, *11*. https://doi.org/10.1029/2018MS001545

Dee, D. P., Balmaseda, M., Balsamo, G., Engelen, R., Simmons, A. J., & Thépaut, J. N. (2014). Toward a consistent reanalysis of the climate system. *Bulletin of the American Meteorological Society*, *95*(8), 1235–1248. https://doi.org/10.1175/BAMS-D-13-00043.1

Déqué, M., Dreveton, C., Braun, A., & Cariolle, D. (1994). The ARPEGE/IFS atmosphere model: A contribution to the French community climate modelling. *Climate Dynamics*, *10*(4-5), 249–266. https://doi.org/10.1007/BF00208992

Derksen, C., & Brown, R. (2012). Spring snow cover extent reductions in the 2008–2012 period exceeding climate model projections. *Geophysical Research Letters*, *39*, L19504. https://doi.org/10.1029/2012GL053387

Deser, C., Simpson, I. R., McKinnon, K. A., & Phillips, A. S. (2017). The Northern Hemisphere extratropical atmospheric circulation response to ENSO: How well do we know it and how do we evaluate models accordingly? *Journal of Climate*, *30*(13), 5059–5082. https://doi.org/10.1175/JCLI-D-16-0844.1

Dommenget, D., & Rezny, M. (2018). A caveat note on tuning in the development of coupled climate models. *Journal of Advances in Modeling Earth Systems*, *10*(1), 78–97. https://doi.org/10.1002/2017MS000947

Donohue, K. A., Tracey, K. L., Watts, D. R., Chidichimo, M. P., & Chereskin, T. K. (2016). Mean Antarctic Circumpolar Current transport measured in Drake Passage. *Geophysical Research Letters*, *43*, 11,760–11,767. https://doi.org/10.1002/2016GL070319

Dufresne, J. L., Foujols, M. A., Denvil, S., Caubel, A., Marti, O., Aumont, O., et al. (2013). Climate change projections using the IPSL-CM5 Earth System Model: From CMIP3 to CMIP5. *Climate Dynamics*, *40*(9-10), 2123–2165. https://doi.org/10.1007/s00382-012-1636-1

Emile-Geay, J., & Madec, G. (2009). Geothermal heating, diapycnal mixing and the abyssal circulation. *Ocean Science*, *5*(2), 203–217. https://doi.org/10.5194/os-5-203-2009

Eyring, V., Arblaster, J. M., Cionni, I., Sedláček, J., Perlwitz, J., Young, P. J., et al. (2013). Long-term ozone changes and associated climate impacts in CMIP5 simulations. *Journal of Geophysical Research: Atmospheres*, *118*, 5029–5060. https://doi.org/10.1002/jgrd.50316

Eyring, V., Bony, S., Meehl, G. A., Senior, C. A., Stevens, B., Stouffer, R. J., & Taylor, K. E. (2016). Overview of the Coupled Model Intercomparison Project Phase 6 (CMIP6) experimental design and organization. *Geoscientific Model Development*, *9*(5), 1937–1958. https://doi.org/10.5194/gmd-9-1937-2016

Fan, Y., & van den Dool, H. (2008). A global monthly land surface air temperature analysis for 1948–present. *Journal of Geophysical Research*, *113*(D1), D01103. https://doi.org/10.1029/2007JD008470

Faroux, S., Kaptué Tchuenté, A. T., Roujean, J.-L., Masson, V., Martin, E., & le Moigne, P. (2013). ECOCLIMAP-II/Europe: a twofold database of ecosystems and surface parameters at 1 km resolution based on satellite information for use in land surface, meteorological and climate models. *Geoscientific Model Development*, *6*(2), 563–582. https://doi.org/10.5194/gmd-6-563-2013

Fetterer F, Knowles K, Meier W, M. Savoie, and A. K. Windnagel (2017) Sea ice index, version 3.0. In: NSIDC. https://nsidc.org/data/G02135/versions/3. Accessed 19 Dec 2018

Flato, G., Marotzke, J., Abiodun, B., et al. (2013). Evaluation of climate models. In Intergovernmental Panel on Climate Change (Ed.), *Climate Change 2013 the Physical Science Basis: Working Group I Contribution to the Fifth Assessment Report of the Intergovernmental Panel on Climate Change* (pp. 741–866). Cambridge: Cambridge University Press.

Fouquart, Y., & Bonnel, B. (1980). Computations of solar heating of the Earth's atmosphere—A new parameterization. *Beitrage zur Phys der Atmosphare*, *53*, 35–62.

Fox-Kemper, B., Danabasoglu, G., Ferrari, R., Griffies, S. M., Hallberg, R. W., Holland, M. M., et al. (2011). Parameterization of mixed layer eddies. III: Implementation and impact in global ocean climate simulations. *Ocean Model*, *39*(1-2), 61–78. https://doi.org/10.1016/j.ocemod.2010.09.002

Ganachaud, A., & Wunsch, C. (2003). Large-scale ocean heat and freshwater transports during the World Ocean Circulation Experiment. *Journal of Climate*, *16*(4), 696–705. https://doi.org/10.1175/1520-0442(2003)016<0696:LSOHAF>2.0.CO;2

Gent, P. R., & Mcwilliams, J. C. (1990). Isopycnal mixing in ocean circulation models. *Journal of Physical Oceanography*, *20*(1), 150–155. https://doi.org/10.1175/1520-0485(1990)020<0150:IMIOCM>2.0.CO;2

Gordon, A. L. (1982). Weddell Deep Water variability. *Journal of Marine Research*, *40*, 199–217.

Gregory, J. M., Ingram, W. J., Palmer, M. A., Jones, G. S., Stott, P. A., Thorpe, R. B., et al. (2004). A new method for diagnosing radiative forcing and climate sensitivity. *Geophysical Research Letters*, *31*, L03205. https://doi.org/10.1029/2003GL018747

Grenfell, T. C., & Maykut, G. A. (1977). The optical properties of ice and snow in the Arctic basin. *Journal of Glaciology*, *18*(80), 445–463. https://doi.org/10.3189/S0022143000021122

Grenier, H., & Bretherton, C. S. (2001). A moist PBL parameterization for large-scale models and its application to subtropical cloud-topped marine boundary layers. *Monthly Weather Review*, *129*(3), 357–377. https://doi.org/10.1175/1520-0493(2001)129<0357:AMPPFL>2.0.CO;2

Guérémy, J. F. (2011). A continuous buoyancy based convection scheme: One- and three-dimensional validation. *Tellus Series A: Dynamic Meteorology and Oceanography*, *63*(4), 687–706. https://doi.org/10.1111/j.1600-0870.2011.00521.x

Gupta, A. S., Jourdain, N. C., Brown, J. N., & Monselesan, D. (2013). Climate drift in the CMIP5 models. *Journal of Climate*, *26*(21), 8597–8615. https://doi.org/10.1175/JCLI-D-12-00521.1

Hansen, J., Sato, M., Kharecha, P., & von Schuckmann, K. (2011). Earth's energy imbalance and implications. *Atmospheric Chemistry and Physics*, *11*(24), 13,421–13,449. https://doi.org/10.5194/acp-11-13421-2011

Harris, I., Jones, P. D., Osborn, T. J., & Lister, D. H. (2014). Updated high-resolution grids of monthly climatic observations—The CRU TS3.10 Dataset. *International Journal of Climatology*, *34*(3), 623–642. https://doi.org/10.1002/joc.3711

Holland, M. M., & Bitz, C. M. (2003). Polar amplification of climate change in coupled models. *Climate Dynamics*, *21*(3-4), 221–232. https://doi.org/10.1007/s00382-003-0332-6

Holte, J., Talley, L. D., Gilson, J., & Roemmich, D. (2017). An Argo mixed layer climatology and database. *Geophysical Research Letters*, *44*, 5618–5626. https://doi.org/10.1002/2017GL073426

Hortal, M., & Simmons, A. J. (1991). Use of reduced Gaussian grids in spectral models. *Monthly Weather Review*, *119*(4), 1057–1074. https://doi.org/10.1175/1520-0493(1991)119<1057:UORGGI>2.0.CO;2

Hourdin, F., Găinusă-Bogdan, A., Braconnot, P., Dufresne, J. L., Traore, A. K., & Rio, C. (2015). Air moisture control on ocean surface temperature, hidden key to the warm bias enigma. *Geophysical Research Letters*, *42*, 10,885–10,893. https://doi.org/10.1002/2015GL066764

Hourdin, F., Grandpeix, J. Y., Rio, C., Bony, S., Jam, A., Cheruy, F., et al. (2013). LMDZ5B: The atmospheric component of the IPSL climate model with revisited parameterizations for clouds and convection. *Climate Dynamics*, *40*(9-10), 2193–2222. https://doi.org/10.1007/s00382-012-1343-y

Hourdin, F., Mauritsen, T., Gettelman, A., Golaz, J. C., Balaji, V., Duan, Q., et al. (2017). The art and science of climate model tuning. *Bulletin of the American Meteorological Society*, *98*(3), 589–602. https://doi.org/10.1175/BAMS-D-15-00135.1

Huang, B., Thorne, P. W., Banzon, V. F., Boyer, T., Chepurin, G., Lawrimore, J. H., et al. (2017). Extended reconstructed sea surface temperature, version 5 (ERSSTv5): Upgrades, validations, and intercomparisons. *Journal of Climate*, *30*(20), 8179–8205. https://doi.org/10.1175/JCLI-D-16-0836.1

Huffman, G. J., Bolvin, D. T., Nelkin, E. J., Wolff, D. B., Adler, R. F., Gu, G., et al. (2007). The TRMM Multisatellite Precipitation Analysis (TMPA): Quasi-global, multiyear, combined-sensor precipitation estimates at fine scales. *Journal of Hydrometeorology*, *8*(1), 38–55. https://doi.org/10.1175/JHM560.1

Hung, M.-P., Lin, J.-L., Wang, W., Kim, D., Shinoda, T., & Weaver, S. J. (2013). MJO and convectively coupled equatorial waves simulated by CMIP5 climate models. *Journal of Climate*, *26*(17), 6185–6214. https://doi.org/10.1175/JCLI-D-12-00541.1

Hunke, E. C., Dukowicz, J. K., Hunke, E. C., & Dukowicz, J. K. (1997). An elastic–viscous–plastic model for sea ice dynamics. *Journal of Physical Oceanography*, *27*(9), 1849–1867. https://doi.org/10.1175/1520-0485(1997)027<1849:AEVPMF>2.0.CO;2

Hunke EC, Lipscomb WH (2010) CICE: The Los Alamos sea ice model documentation and software User's manual LA-CC-06-012

IOC, SCOR, IAPSO (2010) The international thermodynamic equation of seawater—2010: Calculation and use of thermodynamic properties. Intergov Oceanogr Comm Manuals Guid No 56, UNESCO. doi: https://doi.org/10.1109/VETECF.2008.21

Jacobs, S. S., Amos, A. F., & Bruchhausen, P. M. (1970). Ross sea oceanography and antarctic bottom water formation. *Deep Sea Research and Oceanographic Abstracts*, *17*(6), 935–962. https://doi.org/10.1016/0011-7471(70)90046-X

Johns, W. E., Baringer, M. O., Beal, L. M., Cunningham, S. A., Kanzow, T., Bryden, H. L., et al. (2011). Continuous, array-based estimates of Atlantic Ocean heat transport at 26.5°N. *Journal of Climate*, *24*(10), 2429–2449. https://doi.org/10.1175/2010JCLI3997.1

Kato, S., Loeb, N. G., Rose, F. G., Doelling, D. R., Rutan, D. A., Caldwell, T. E., et al. (2013). Surface irradiances consistent with CERES-derived top-of-atmosphere shortwave and longwave irradiances. *Journal of Climate*, *26*(9), 2719–2740. https://doi.org/10.1175/JCLI-D-12-00436.1

Knutti, R., Rugenstein, M. A. A., & Hegerl, G. C. (2017). Beyond equilibrium climate sensitivity. *Nature Geoscience*, *10*(10), 727–736. https://doi.org/10.1038/ngeo3017

Kourzeneva, E. (2010). External data for lake parameterization in numerical weather prediction and climate modeling. *Boreal Environment Research*, *64*(1), 15640. https://doi.org/10.3402/tellusa.v64i0.15640

Landerer, F. W., & Swenson, S. C. (2012). Accuracy of scaled GRACE terrestrial water storage estimates. *Water Resources Research*, *48*, W04531. https://doi.org/10.1029/2011WR011453

Large, W. G., & Yeager, S. G. (2009). The global climatology of an interannually varying air-sea flux data set. *Climate Dynamics*, *33*(2-3), 341–364. https://doi.org/10.1007/s00382-008-0441-3

Le Moigne, P., Colin, J., & Decharme, B. (2016). Impact of lake surface temperatures simulated by the FLake scheme in the CNRM-CM5 climate model. *Tellus A: Dynamic Meteorology and Oceanography*, *68*(1), 31274. https://doi.org/10.3402/tellusa.v68.31274

Lee, Y. J., Matrai, P. A., Friedrichs, M. A. M., Saba, V. S., Aumont, O., Babin, M., et al. (2016). Net primary productivity estimates and environmental variables in the Arctic Ocean: An assessment of coupled physical-biogeochemical models. *Journal of Geophysical Research: Oceans*, *121*, 8635–8669. https://doi.org/10.1002/2016JC011993

Lengaigne, M., Menkes, C., Aumont, O., Gorgues, T., Bopp, L., André, J. M., & Madec, G. (2007). Influence of the oceanic biology on the tropical Pacific climate in a coupled general circulation model. *Climate Dynamics*, *28*(5), 503–516. https://doi.org/10.1007/s00382-006-0200-2

Leroux, S., Bellon, G., Roehrig, R., Caian, M., Klingaman, N. P., Lafore, J. P., et al. (2016). Inter-model comparison of subseasonal tropical variability in aquaplanet experiments: Effect of a warm pool. *Journal of Advances in Modeling Earth Systems*, *8*, 1526–1551. https://doi.org/10.1002/2016MS000683

Liebmann, B., & Smith, C. A. (1996). Description of a complete (interpolated) outgoing longwave radiation dataset. *Bulletin of the American Meteorological Society*, *77*, 1275–1277.

Locarnini RA, Mishonov A. V., Antonov JI, T. P. Boyer, H. E. Garcia, O. K. Baranova, et al. (2013) World Ocean Atlas 2013. Vol. *1*: *Temperature*. In: S. Levitus, Ed.; A. Mishonov, Technical Ed.; NOAA Atlas NESDIS, *73*, 40 pp, https://data.nodc.noaa.gov/woa/WOA13/DOC/woa13_vol1.pdf

Loeb, N. G., Wielicki, B. A., Doelling, D. R., Smith, G. L., Keyes, D. F., Kato, S., et al. (2009). Toward optimal closure of the Earth's top-of-atmosphere radiation budget. *Journal of Climate*, *22*(3), 748–766. https://doi.org/10.1175/2008JCLI2637.1

Lopez, P. (2002). Implementation and validation of a new prognostic large-scale cloud and precipitation scheme for climate and data-assimilation purposes. *Quarterly Journal of the Royal Meteorological Society*, *128*(579), 229–257. https://doi.org/10.1256/00359000260498879

Lott, F., Guez, L., & Maury, P. (2012). A stochastic parameterization of non-orographic gravity waves: Formalism and impact on the equatorial stratosphere. *Geophysical Research Letters*, *39*, L06807. https://doi.org/10.1029/2012GL051001

Lucarini, V., & Ragone, F. (2011). Energetics of climate models: Net energy balance and meridional enthalpy transport. *Reviews of Geophysics*, *49*, RG1001. https://doi.org/10.1029/2009RG000323

Madden, R. A., & Julian, P. R. (1971). Detection of a 40–50 day oscillation in the zonal wind in the tropical pacific. *Journal of the Atmospheric Sciences*, *28*(5), 702–708. https://doi.org/10.1175/1520-0469(1971)028<0702:DOADOI>2.0.CO;2

Madec G, Bourdallé-Badie R, Bouttier P-A, Clément Bricaud, Diego Bruciaferri, Daley Calvert, et al. (2017). NEMO ocean engine. https://doi.org/10.5281/ZENODO.1472492

Madec, G., Delécluse, P., Imbard, M., & Lévy, C. (1998). OPA 8.1 Ocean General Circulation Model reference manual. Note du Pôle modélisation. *Inst Pierre-Simon Laplace*, *11*, 1–91.

Masson, V., Le Moigne, P., Martin, E., et al. (2013). The SURFEXv7.2 land and ocean surface platform for coupled or offline simulation of earth surface variables and fluxes. *Geoscientific Model Development*, *6*(4), 929–960. https://doi.org/10.5194/gmd-6-929-2013

Mathiot, P., Jenkins, A., Harris, C., & Madec, G. (2017). Explicit representation and parametrised impacts of under ice shelf seas in the z^* coordinate ocean model NEMO 3.6. *Geoscientific Model Development*, *10*(7), 2849–2874. https://doi.org/10.5194/gmd-10-2849-2017

Matthes, K., Funke, B., Andersson, M. E., Barnard, L., Beer, J., Charbonneau, P., et al. (2017). Solar forcing for CMIP6 (v3.2). *Geoscientific Model Development*, *10*(6), 2247–2302. https://doi.org/10.5194/gmd-10-2247-2017

McCarthy, G., Smeed, D., Cunningham, S., & Roberts, C. (2017). Atlantic Meridonal Overturning Circulation (AMOC). In *Marine Climate Change Impacts Partnership: Science Review: MCCIP Science Review 2017* (pp. 15–21). https://doi.org/10.14465/2017.arc10.002-atl

McPhee, M. G. (1992). Turbulent heat flux in the upper ocean under sea ice. *Journal of Geophysical Research*, *97*(C4), 5365–5379. https://doi.org/10.1029/92JC00239

Mechoso, C. R., Losada, T., Koseki, S., Mohino-Harris, E., Keenlyside, N., Castaño-Tierno, A., et al. (2016). Can reducing the incoming energy flux over the Southern Ocean in a CGCM improve its simulation of tropical climate? *Geophysical Research Letters*, *43*, 11,057–11,063. https://doi.org/10.1002/2016GL071150

Meinshausen, M., Vogel, E., Nauels, A., Lorbacher, K., Meinshausen, N., Etheridge, D. M., et al. (2017). Historical greenhouse gas concentrations for climate modelling (CMIP6). *Geoscientific Model Development*, *10*(5), 2057–2116. https://doi.org/10.5194/gmd-10-2057-2017

Meurdesoif Y (2018) Xios fortran reference guide. IPSL, http://forge.ipsl.jussieu.fr/ioserver/svn/XIOS/trunk/doc/XIOS_reference_guide.pdf

Michou, M., Nabat, P., & Saint-Martin, D. (2015). Development and basic evaluation of a prognostic aerosol scheme (v1) in the CNRM Climate Model CNRM-CM6. *Geoscientific Model Development*, *8*(3), 501–531. https://doi.org/10.5194/gmd-8-501-2015

Mignot, J., Swingedouw, D., Deshayes, J., Marti, O., Talandier, C., Séférian, R., et al. (2013). On the evolution of the oceanic component of the IPSL climate models from CMIP3 to CMIP5: A mean state comparison. *Ocean Model*, *72*, 167–184. https://doi.org/10.1016/j.ocemod.2013.09.001

Miller, R. L., Schmidt, G. A., & Shindell, D. T. (2006). Forced annular variations in the 20th century Intergovernmental Panel on Climate Change Fourth Assessment Report models. *Journal of Geophysical Research*, *111*(D18), D18101. https://doi.org/10.1029/2005JD006323

Mlawer, E. J., Taubman, S. J., Brown, P. D., Iacono, M. J., & Clough, S. A. (1997). Radiative transfer for inhomogeneous atmospheres: RRTM, a validated correlated-k model for the longwave. *Journal of Geophysical Research*, *102*(D14), 16,663–16,682. https://doi.org/10.1029/97JD00237

Monge-Sanz, B. M., Chipperfield, M. P., Cariolle, D., & Feng, W. (2011). Results from a new linear O_3 scheme with embedded heterogeneous chemistry compared with the parent full-chemistry 3-D CTM. *Atmospheric Chemistry and Physics*, *11*(3), 1227–1242. https://doi.org/10.5194/acp-11-1227-2011

Morel, A., & Berthon, J. –. F. (1989). Surface pigments, algal biomass profiles, and potential production of the euphotic layer: Relationships reinvestigated in view of remote-sensing applications. *Limnology and Oceanography*, *34*(8), 1545–1562. https://doi.org/10.4319/lo.1989.34.8.1545

Morgenstern, O., Hegglin, M., Rozanov, E., O'Connor, F. M., Abraham, N. L., Akiyoshi, H., et al. (2017). Review of the global models used within phase 1 of the Chemistry-Climate Model Initiative (CCMI). *Geoscientific Model Development*, *10*(2), 639–671. https://doi.org/10.5194/gmd-10-639-2017

Morice, C. P., Kennedy, J. J., Rayner, N. A., & Jones, P. D. (2012). Quantifying uncertainties in global and regional temperature change using an ensemble of observational estimates: The HadCRUT4 data set. *Journal of Geophysical Research*, *117*, D08101. https://doi.org/10.1029/2011JD017187

Mudryk, L. R., Derksen, C., Howell, S., Laliberté, F., Thackeray, C., Sospedra-Alfonso, R., et al. (2018). Canadian snow and sea ice: Historical trends and projections. *The Cryosphere*, *12*(4), 1157–1176. https://doi.org/10.5194/tc-12-1157-2018

Mudryk, L. R., Kushner, P. J., Derksen, C., & Thackeray, C. (2017). Snow cover response to temperature in observational and climate model ensembles. *Geophysical Research Letters*, *44*, 919–926. https://doi.org/10.1002/2016GL071789

Mueller, B., & Seneviratne, S. I. (2014). Systematic land climate and evapotranspiration biases in CMIP5 simulations. *Geophysical Research Letters*, *41*, 128–134. https://doi.org/10.1002/2013GL058055

Muller, R., Rohde, R., Jacobsen, R., Muller, E., & Wickham, C. (2013). A new estimate of the average Earth surface land temperature spanning 1753 to 2011. *Geoinformatics Geostatistics An Overview*, *01*, 1–7. https://doi.org/10.4172/2327-4581.1000101

Myhre, G., Shindell, D., Bréon, F.-M., et al. (2013). Fifth Assessment Report of the Intergovernmental Panel on Climate Change—Chapter 8: Anthropogenic and natural radiative forcing. In T. F. Stocker, D. Qin, G.-K. Plattner, M. Tignor, S. K. Allen, J. Boschung, A. Nauels, Y. Xia, V. Bex, & P. M. Midgley (Eds.), *Climate Change 2013: The Physical Science Basis. Contribution of Working Group I to the Fifth Assessment Report of the Intergovernmental Panel on Climate Change* (pp. 659–740). Cambridge, United Kingdom and New York, NY, USA: Cambridge University Press. https://doi.org/10.1017/CBO9781107415324.018

Nam, C., Bony, S., Dufresne, J.-L., & Chepfer, H. (2012). The 'too few, too bright' tropical low-cloud problem in CMIP5 models. *Geophysical Research Letters*, *39*, 21801. https://doi.org/10.1029/2012GL053421

Nguyen, H., Evans, A., Lucas, C., Smith, I., & Timbal, B. (2013). The Hadley circulation in reanalyses: Climatology, variability, and Change. *Journal of Climate*, *26*(10), 3357–3376. https://doi.org/10.1175/JCLI-D-12-00224.1

Nidheesh, A. G., Lengaigne, M., Vialard, J., Izumo, T., Unnikrishnan, A. S., & Cassou, C. (2017). Influence of ENSO on the Pacific decadal oscillation in CMIP models. *Climate Dynamics*, *49*(9-10), 3309–3326. https://doi.org/10.1007/s00382-016-3514-8

Noilhan, J., & Planton, S. (1989). A simple parameterization of land surface processes for meteorological models. *Monthly Weather Review*, *117*(3), 536–549. https://doi.org/10.1175/1520-0493(1989)117<0536:ASPOLS>2.0.CO;2

Notz, D. (2005). *Thermodynamic and fluid-dynamical processes in sea ice*. Cambridge: University of Cambridge.

Oki, T., & Sud, Y. C. (1998). Design of Total Runoff Integrating Pathways (TRIP)—A global river channel network. *Earth Interactions*, *2*(1), 1–37. https://doi.org/10.1175/1087-3562(1998)002<0001:DOTRIP>2.3.CO;2

Peings, Y., Brun, E., Mauvais, V., & Douville, H. (2013). How stationary is the relationship between Siberian snow and Arctic Oscillation over the 20th century? *Geophysical Research Letters*, *40*, 183–188. https://doi.org/10.1029/2012GL054083

Piriou, J.-M., Redelsperger, J.-L., Geleyn, J.-F., Lafore, J. P., & Guichard, F. (2007). An approach for convective parameterization with memory: Separating microphysics and transport in grid-scale equations. *Journal of the Atmospheric Sciences*, *64*(11), 4127–4139. https://doi.org/10.1175/2007JAS2144.1

Qasmi, S., Cassou, C., & Boé, J. (2017). Teleconnection between Atlantic multidecadal variability and European temperature: Diversity and evaluation of the Coupled Model Intercomparison Project Phase 5 Models. *Geophysical Research Letters*, *44*, 11,140–11,149. https://doi.org/10.1002/2017GL074886

Rayner, N. A., Parker, D. E., Horton, E. B., Folland, C. K., Alexander, L. V., Rowell, D. P., et al. (2003). Global analyses of sea surface temperature, sea ice, and night marine air temperature since the late nineteenth century. *Journal of Geophysical Research*, *108*(D14), 4407. https://doi.org/10.1029/2002JD002670

Ricard, J. L., & Royer, J. F. (1993). A statistical cloud scheme for use in an AGCM. *Annales de Geophysique*, *11*, 1095–1115.

Richter, I. (2015). Climate model biases in the eastern tropical oceans: Causes, impacts and ways forward. *Wiley Interdisciplinary Reviews: Climate Change*, *6*(3), 345–358. https://doi.org/10.1002/wcc.338

Rienecker, M. M., Suarez, M. J., Gelaro, R., Todling, R., Bacmeister, J., Liu, E., et al. (2011). MERRA: NASA's Modern-Era Retrospective Analysis for Research and Applications. *Journal of Climate*, *24*(14), 3624–3648. https://doi.org/10.1175/JCLI-D-11-00015.1

Rohde, R., Muller, R., Jacobsen, R., Perlmutter, S., Rosenfeld, A., Wurtele, J., et al. (2013). Berkeley Earth temperature averaging process. Geoinfor Geostat: An overview 1: 2. *Geoinformatics Geostatistics An Overview*, *1*(2), 20–100. https://doi.org/10.4172/2327-4581.1000103

Roquet, F., Madec, G., McDougall, T. J., & Barker, P. M. (2015). Accurate polynomial expressions for the density and specific volume of seawater using the TEOS-10 standard. *Ocean Model*, *90*, 29–43. https://doi.org/10.1016/J.OCEMOD.2015.04.002

Roy, F., Chevallier, M., Smith, G. C., Dupont, F., Garric, G., Lemieux, J. F., et al. (2015). Arctic sea ice and freshwater sensitivity to the treatment of the atmosphere-ice-ocean surface layer. *Journal of Geophysical Research: Oceans*, *120*, 4392–4417. https://doi.org/10.1002/2014JC010677

Ruprich-Robert, Y., & Cassou, C. (2015). Combined influences of seasonal East Atlantic Pattern and North Atlantic Oscillation to excite Atlantic multidecadal variability in a climate model. *Climate Dynamics*, *44*, 229–253. https://doi.org/10.1007/s00382-014-2176-7

Ruprich-Robert, Y., Msadek, R., Castruccio, F., Yeager, S., Delworth, T., & Danabasoglu, G. (2017). Assessing the climate impacts of the observed Atlantic multidecadal variability using the GFDL CM2.1 and NCAR CESM1 global coupled models. *Journal of Climate*, *30*(8), 2785–2810. https://doi.org/10.1175/JCLI-D-16-0127.1

Salas Mélia, D. (2002). A global coupled sea ice–ocean model. *Ocean Modelling*, *4*(2), 137–172. https://doi.org/10.1016/S1463-5003(01)00015-4

Schneider, U., Becker, A., Finger, P., Meyer-Christoffer, A., Ziese, M., & Rudolf, B. (2014). GPCC's new land surface precipitation climatology based on quality-controlled in situ data and its role in quantifying the global water cycle. *Theoretical and Applied Climatology*, *115*(1-2), 15–40. https://doi.org/10.1007/s00704-013-0860-x

Schuur, E. A. G., McGuire, A. D., Schädel, C., Grosse, G., Harden, J. W., Hayes, D. J., et al. (2015). Climate change and the permafrost carbon feedback. *Nature*, *520*(7546), 171–179. https://doi.org/10.1038/nature14338

Séférian, R., Baek, S., Boucher, O., Dufresne, J. L., Decharme, B., Saint-Martin, D., & Roehrig, R. (2018). An interactive ocean surface albedo scheme (OSAv1.0): Formulation and evaluation in ARPEGE-Climat (V6.1) and LMDZ (V5A). *Geoscientific Model Development*, *11*(1), 321–338. https://doi.org/10.5194/gmd-11-321-2018

Shchepetkin, A. F., & McWilliams, J. C. (2005). The regional oceanic modeling system (ROMS): A split-explicit, free-surface, topography-following-coordinate oceanic model. *Ocean Modelling*, *9*(4), 347–404. https://doi.org/10.1016/j.ocemod.2004.08.002

Sherwood, S. C., Bony, S., & Dufresne, J.-L. (2014). Spread in model climate sensitivity traced to atmospheric convective mixing. *Nature*, *505*(7481), 37–42. https://doi.org/10.1038/nature12829

Sommeria, G., & Deardorff, J. W. (1977). Subgrid-scale condensation in models of nonprecipitating clouds. *Journal of the Atmospheric Sciences*, *34*(2), 344–355. https://doi.org/10.1175/1520-0469(1977)034<0344:SSCIMO>2.0.CO;2

Stachnik, J. P., & Schumacher, C. (2011). A comparison of the Hadley circulation in modern reanalyses. *Journal of Geophysical Research*, *116*, D22102. https://doi.org/10.1029/2011JD016677

Stocker, T. F., Qin, D., Plattner, G.-K., Tignor, M., Allen, S. K., Boschung, J., et al. (2013). Technical summary. In *Climate Change 2013 the Physical Science Basis: Working Group I Contribution to the Fifth Assessment Report of the Intergovernmental Panel on Climate Change* (pp. 33–115). Cambridge, UK: Cambridge University Press.

Swenson SC (2012) GRACE monthly land water mass grids NETCDF RELEASE 5.0. PO DAAC, CA, USA

Szopa, S., Balkanski, Y., Schulz, M., Bekki, S., Cugnet, D., Fortems-Cheiney, A., et al. (2013). Aerosol and ozone changes as forcing for climate evolution between 1850 and 2100. *Climate Dynamics*, *40*(9-10), 2223–2250. https://doi.org/10.1007/s00382-012-1408-y

Thomason, L. W., Ernest, N., Millán, L., Rieger, L., Bourassa, A., Vernier, J. P., et al. (2018). A global space-based stratospheric aerosol climatology: 1979–2016. *Earth System Science Data*, *10*(1), 469–492. https://doi.org/10.5194/essd-10-469-2018

Ting, M., Kushnir, Y., Seager, R., & Li, C. (2009). Forced and internal twentieth-century SST trends in the North Atlantic*. *Journal of Climate*, *22*(6), 1469–1481. https://doi.org/10.1175/2008JCLI2561.1

Trenberth, K. E., & Caron, J. M. (2001). Estimates of meridional atmosphere and ocean heat transports. *Journal of Climate*, *14*(16), 3433–3443. https://doi.org/10.1175/1520-0442(2001)014<3433:EOMAAO>2.0.CO;2

Trenberth, K. E., & Fasullo, J. T. (2010). Simulation of present-day and twenty-first-century energy budgets of the Southern Oceans. *Journal of Climate*, *23*(2), 440–454. https://doi.org/10.1175/2009JCLI3152.1

Valcke, S., Guilyardi, E., & Larsson, C. (2006). PRISM and ENES: A European approach to Earth system modelling. *Concurrency and Computation: Practice and Experience*, *18*(2), 247–262. https://doi.org/10.1002/CPE.V18:2

Vancoppenolle, M., Fichefet, T., Goosse, H., Bouillon, S., Madec, G., & Maqueda, M. A. M. (2009). Simulating the mass balance and salinity of Arctic and Antarctic sea ice. 1. Model description and validation. *Ocean Model*, *27*(1-2), 33–53. https://doi.org/10.1016/J.OCEMOD.2008.10.005

Voldoire, A., Decharme, B., Pianezze, J., Lebeaupin Brossier, C., Sevault, F., Seyfried, L., et al. (2017). SURFEX v8.0 interface with OASIS3-MCT to couple atmosphere with hydrology, ocean, waves and sea-ice models, from coastal to global scales. *Geoscientific Model Development*, *10*(11), 4207–4227. https://doi.org/10.5194/gmd-10-4207-2017

Voldoire, A., Sanchez-Gomez, E., Salas y Mélia, D., Decharme, B., Cassou, C., Sénési, S., et al. (2013). The CNRM-CM5.1 global climate model: Description and basic evaluation. *Climate Dynamics*, *40*(9-10), 2091–2121. https://doi.org/10.1007/s00382-011-1259-y

Waliser, D., Hendon, H., Kim, D., et al. (2009). MJO simulation diagnostics. *Journal of Climate*, *22*(11), 3006–3030. https://doi.org/10.1175/2008JCLI2731.1

Wang, C., Zhang, L., Lee, S. K., Wu, L., & Mechoso, C. R. (2014). A global perspective on CMIP5 climate model biases. *Nature Climate Change*, *4*(3), 201–205. https://doi.org/10.1038/nclimate2118

Watson, L., Michou, M., Nabat, P., & Saint-Martin, D. (2018). Assessment of CNRM coupled ocean-atmosphere model sensitivity to the representation of aerosols. *Climate Dynamics*, *51*(7-8), 2877–2895. https://doi.org/10.1007/s00382-017-4054-6

Wheeler, M., & Kiladis, G. N. (1999). Convectively coupled equatorial waves: Analysis of clouds and temperature in the wavenumber–frequency domain. *Journal of the Atmospheric Sciences*, *56*(3), 374–399. https://doi.org/10.1175/1520-0469(1999)056<0374:CCEWAO>2.0.CO;2

Winton, M., Anderson, W. G., Delworth, T. L., Griffies, S. M., Hurlin, W. J., & Rosati, A. (2014). Has coarse ocean resolution biased simulations of transient climate sensitivity? *Geophysical Research Letters*, *41*, 8522–8529. https://doi.org/10.1002/2014GL061523

Woods, C., Caballero, R., & Svensson, G. (2017). Representation of Arctic moist intrusions in CMIP5 models and implications for winter climate biases. *Journal of Climate*, *30*(11), 4083–4102. https://doi.org/10.1175/JCLI-D-16-0710.1

Zhang, C. (2005). Madden-Julian Oscillation. *Reviews of Geophysics*, *43*, RG2003. https://doi.org/10.1029/2004RG000158

Zhang, J., & Rothrock, D. A. (2003). Modeling global sea ice with a thickness and enthalpy distribution model in generalized curvilinear coordinates. *Monthly Weather Review*, *131*(5), 845–861. https://doi.org/10.1175/1520-0493(2003)131<0845:MGSIWA>2.0.CO;2

Zuidema, P., Chang, P., Medeiros, B., Kirtman, B. P., Mechoso, R., Schneider, E. K., et al. (2016). Challenges and prospects for reducing coupled climate model sst biases in the eastern tropical atlantic and pacific oceans: The U.S. Clivar eastern tropical oceans synthesis working group. *Bulletin of the American Meteorological Society*, *97*(12), 2305–2328. https://doi.org/10.1175/BAMS-D-15-00274.1

Erratum

In the originally published version of this article, the name of author L. Franchistéguy was misspelled as "L. Franchistguy." The error has been corrected, and this may be considered the official version of record.